

**Centriolar satellites expedite mother centriole remodeling to promote ciliogenesis.**

Emma A. Hall<sup>\*1</sup>, Dhivya Kumar<sup>\*2</sup>, Suzanna L. Prosser<sup>3</sup>, Patricia L. Yeyati<sup>1</sup>, Vicente Herranz Pérez<sup>4,5</sup>, Jose Manuel García Verdugo<sup>4</sup>, Lorraine Rose<sup>1</sup>, Lisa McKie<sup>1</sup>, Daniel O. Dodd<sup>1</sup>, Peter A. Tennant<sup>1</sup>, Roly Megaw<sup>1</sup>, Laura C. Murphy<sup>6</sup>, Marisa F. Ferreira<sup>1</sup>, Graeme Grimes<sup>1</sup>, Lucy Williams<sup>1</sup>, Tooba Quidwai<sup>1</sup>, Laurence Pelletier<sup>3,7</sup>, Jeremy F. Reiter<sup>‡2,8</sup>, Pleasantine Mill<sup>‡1</sup>

<sup>\*</sup> Authors contributed equally

<sup>‡</sup> Corresponding authors

1. MRC Human Genetics Unit, Institute of Genetics and Cancer, University of Edinburgh, Edinburgh, UK, EH4 2XU
2. Department of Biochemistry and Biophysics, Cardiovascular Research Institute, University of California, San Francisco, San Francisco, CA 94143, USA
3. Lunenfeld-Tanenbaum Research Institute, Sinai Health System, 600 University Avenue, Toronto, ON M5G 1X5, Canada
4. Cavanilles Institute of Biodiversity and Evolutionary Biology, University of Valencia, 46010, Valencia, Spain
5. Predepartamental Unit of Medicine, Jaume I University, 12006 Castelló de la Plana, Spain
6. Institute of Genetics and Cancer, University of Edinburgh, Edinburgh, UK, EH4 2XU
7. Department of Molecular Genetics, University of Toronto, Toronto, ON, M5S 1A8 Canada
8. Chan Zuckerberg Biohub, San Francisco, CA 94158, USA

**Abstract**

Centrosomes are orbited by centriolar satellites, dynamic multiprotein assemblies nucleated by Pericentriolar Material 1 (PCM1). To study the requirement for centriolar satellites, we generated mice lacking PCM1, a crucial component of satellites. *Pcm1*<sup>-/-</sup> mice display partially penetrant perinatal lethality with survivors exhibiting hydrocephalus, oligospermia and cerebellar hypoplasia, and variably expressive phenotypes such as hydronephrosis. As many of these phenotypes have been observed in human ciliopathies and satellites are implicated in cilia biology, we investigated whether cilia were affected. PCM1 was dispensable for ciliogenesis in many cell types, whereas *Pcm1*<sup>-/-</sup> multiciliated ependymal cells and human *PCM1*<sup>-/-</sup> retinal pigmented epithelial 1 (RPE1) cells showed reduced ciliogenesis. *PCM1*<sup>-/-</sup> RPE1 cells displayed reduced docking of the mother centriole to the

---

36 ciliary vesicle and removal of CP110 and CEP97 from the distal mother centriole, indicating  
37 compromised early ciliogenesis. Similarly, *Pcm1*<sup>-/-</sup> ependymal cells exhibited reduced  
38 removal of CP110 from basal bodies *in vivo*. We propose that PCM1 and centriolar satellites  
39 facilitate efficient trafficking of proteins to and from centrioles, including the departure of  
40 CP110 and CEP97 to initiate ciliogenesis, and that the threshold to trigger ciliogenesis  
41 differs between cell types.

42

43

44

45

46

---

## 47    **Introduction**

48            A pair of microtubule-based centrioles form the heart of the centrosome. In addition  
49 to roles in spindle formation during mitosis, centrioles are critical to ciliogenesis, the process  
50 of building a cilium during interphase (Nigg and Holland, 2018). In most cells, the older  
51 mother centriole uniquely matures into the basal body, which serves as the foundation for  
52 the primary cilium, a single signaling antenna. In contrast, multiciliated cells lining the  
53 trachea, oviduct and brain ventricles generate many basal bodies that then nucleate many  
54 motile cilia per cell.

55            In all cells, dynamic remodeling of centrioles is required for ciliogenesis. Key early  
56 steps in ciliogenesis include basal body acquisition of distal appendages and the removal of  
57 CP110 and CEP97 from the distal end of the mother centriole, two proteins that inhibit  
58 assembly of the ciliary axoneme (Čajánek and Nigg, 2014; Goetz et al., 2012; Schmidt et al.,  
59 2012, 2009; Sillibourne et al., 2013; Spektor et al., 2007; Tanos et al., 2013; Tsang et al.,  
60 2008). How the cell controls centriole remodeling remains unclear.

61            Surrounding the centrosome and ciliary base are centriolar satellites, small  
62 membrane-less granules which move along cytoplasmic microtubules (Bärenz et al., 2011;  
63 Kubo et al., 1999; Kubo and Tsukita, 2003; Odabasi et al., 2020). PCM1 is both a  
64 component of centriolar satellites and necessary for centriolar satellite formation  
65 (Dammermann and Merdes, 2002; Kubo and Tsukita, 2003; Odabasi et al., 2019; Wang et  
66 al., 2016). With PCM1, a diverse array of proteins co-localize at centriolar satellites  
67 (Gheiratmand et al., 2019; Gupta et al., 2015; Odabasi et al., 2019; Quarantotti et al., 2019),  
68 and many of these components also localize at centrioles themselves (Kodani et al., 2015;  
69 Lopes et al., 2011). Centriolar satellites are dynamic, change in response to cell stresses, and  
70 have been implicated in diverse processes including Hedgehog signaling, autophagy,  
71 proteasome activity and aggresome formation (Holdgaard et al., 2019; Hori and Toda, 2017;  
72 Joachim et al., 2017; Kubo and Tsukita, 2003; Lecland and Merdes, 2018; Odabasi et al.,  
73 2019; Prosser et al., 2022; Prosser and Pelletier, 2020; Tang et al., 2013; Tollenaere et al.,  
74 2015; Villumsen et al., 2013; G. Wang et al., 2013). Possibly reflecting involvement in these  
75 diverse biological processes, genetic perturbation of centriolar satellite components can  
76 compromise cilia formation and contribute to human ciliopathies and microcephaly (Conkar  
77 et al., 2017; Kim et al., 2008; Klinger et al., 2014; Kurtulmus et al., 2016; Lee and Stearns,  
78 2013; Mikule et al., 2007; Staples et al., 2014), perhaps in a cell-type specific way (Monroe et  
79 al., 2020; Odabasi et al., 2019; Wang et al., 2016). Thus, understanding of the function of  
80 PCM1 and centriolar satellites is emerging.

---

81           To investigate the functions of centriolar satellites *in vivo*, we generated *Pcm1* null  
82 mice. We found that PCM1 is important for perinatal survival. *Pcm1*<sup>-/-</sup> mice surviving the  
83 perinatal period displayed dwarfism, male infertility, hydrocephaly, cerebellar hypoplasia and  
84 variably expressive ciliopathy-associated phenotypes such as hydronephrosis, reflecting  
85 important roles for centriolar satellites in promoting both primary and motile ciliogenesis. In  
86 assessing how centriolar satellites enable ciliogenesis, we found that cells lacking PCM1  
87 display compromised docking of the mother centriole to the ciliary vesicle and attenuated  
88 removal of CP110 and CEP97. Thus, we propose that centriolar satellites shape the mother  
89 centriole to promote critical early steps in ciliogenesis.

90

91

92

---

## Results

### ***Pcm1*<sup>-/-</sup> mice exhibit perinatal lethality and ciliopathy-associated phenotypes.**

To investigate the *in vivo* function of centriolar satellites in mammals, we used CRISPR/Cas9 to create deletions in mouse *Pcm1*. Among the mutations generated, *Pcm1*<sup>Δ5-14</sup> introduced a frameshift after the first amino acid leading to a premature stop and *Pcm1*<sup>Δ796-800</sup> caused a frameshift and premature stop in exon 6 (**Figure 1 - figure supplement 1A**). Immunoblotting with antibodies to two regions of PCM1, PCM1 immunofluorescence of mouse embryonic fibroblasts (MEFs) derived from *Pcm1* mutant mice, and mass spectrometry-based proteomic analysis indicated that both mutations prevented formation of detectable PCM1 protein (**Figure 1A, B, Figure 1 - figure supplement 1B, C**). Mice homozygous for either *Pcm1* mutation exhibited indistinguishable phenotypes (**Figure 1 - figure supplement 2**). Thus, we surmise that both mutations are likely to be null and henceforth we refer to both alleles as *Pcm1*<sup>-</sup>.

*Pcm1*<sup>-/-</sup> mice were present at normal Mendelian ratios at late gestation (embryonic day [E] 18.5) (**Figure 1C, D, Figure 1- figure supplement 1D**). As abrogation of cilia themselves results in midgestation lethality (Huangfu et al., 2003), the presence of *Pcm1*<sup>-/-</sup> embryos late in gestation suggests that PCM1 is not essential for all ciliogenesis. Indeed, cilia in several *Pcm1*<sup>-/-</sup> tissues were morphologically normal at E18.5 (**Figure 1 - figure supplement 3A-E**). However, by postnatal day (P) 5, half of *Pcm1*<sup>-/-</sup> mice had died (**Figure 1D, Figure 1 - figure supplement 1D**), revealing that PCM1 is important for perinatal survival.

Surviving *Pcm1*<sup>-/-</sup> mice were smaller than littermate controls, weighing less than half of controls at P28 (**Figure 1E, F**). This dwarfism was detectable before birth, indicating intrauterine growth retardation (**Figure 1 - figure supplement 1E**). The brains of surviving *Pcm1*<sup>-/-</sup> mice were proportionally smaller than those of littermates (**Figure 1 - figure supplement 1F, G**), and displayed marked hydrocephaly (**Figure 2 A-C, Figure 2 - figure supplement 1A, B**). Hydrocephaly can result from motile cilia dysfunction, raising the possibility that centriolar satellites are required for cilia formation and/or function in ependymal cells.

In the postnatal brain, primary cilia are critical for Hedgehog signaling in cerebellar granule cell precursors. Decreased cerebellar Hedgehog signaling attenuates expansion of the granule cell precursors (Dahmane and Ruiz i Altaba, 1999; Spassky et al., 2008; Wallace, 1999; Wechsler-Reya and Scott, 1999). The cerebella of *Pcm1*<sup>-/-</sup> mice were smaller than those of littermate controls (**Figure 2D-F, Figure 2 - figure supplement 1A**). As the

cerebellum is important for motor coordination, we analyzed the gait of surviving *Pcm1*<sup>-/-</sup> mice. Consistent with altered cerebellar function, *Pcm1*<sup>-/-</sup> mice displayed ataxia (**Figure 2G**).

We investigated whether *Pcm1*<sup>-/-</sup> mice exhibit other Hedgehog-associated phenotypes. A proportion of viable *Pcm1*<sup>-/-</sup> mice (n=2/15) developed hydronephrosis (**Figure 2H**), which can also result from attenuated Hedgehog signaling (Yu et al., 2002).

Because retinal degeneration is characteristic of several ciliopathies and PCM1 was strongly expressed in the retina (**Figure 2 - figure supplement 1 D**), we examined the retinas of *Pcm1*<sup>-/-</sup> mice using fundal imaging and histological analysis at one year of age. *Pcm1*<sup>-/-</sup> mice did not display characteristic features of photoreceptor death, such as changes to retinal pigmentation on funduscopy or reduction of the outer nuclear layer on histology (**Figure 2 - figure supplement 1 E, F**). Electroretinogram (ERG) testing at 9 months of age revealed no visual functional deficits in *Pcm1*<sup>-/-</sup> mice (**Figure 2 - figure supplement 1 G-I**). Therefore, PCM1 is not essential for photoreceptor survival, suggesting it is dispensable for photoreceptor ciliogenesis and ciliary trafficking.

Surviving *Pcm1*<sup>-/-</sup> male mice were infertile with reduced sperm in seminiferous tubules (**Figure 2I-K, Figure 2 - figure supplement 1C**). The few *Pcm1*<sup>-/-</sup> sperm identified exhibited disrupted head-to-tail coupling, abnormal head morphology indicative of defective intramanchette trafficking, and immotility (**Figure 2 - figure supplement 1C, Figure 2 – videos 1-3**). We previously discovered similar defects in male mice lacking centriolar satellite component CEP131 (also known as AZ11) (Hall et al., 2013), consistent with the idea that centriolar satellites are essential for mammalian spermatogenesis and male fertility. Thus, PCM1 supports postnatal survival and is required for the function of multiple ciliated cell types.

## **PCM1 promotes ciliogenesis in multiciliated cells.**

During the perinatal period, ependymal cells lining the brain ventricles generate many motile cilia. Shortly after birth (P1), immature ependymal cells possess non-polarized, short cilia. Beginning at P3, ependymal cells form multiple long, polarized cilia; this ciliogenesis occurs in a wave across the ventricle from caudal to rostral. By P15, ependymal cilia mature to generate metachronal rhythm (Spassky et al., 2008). Recent work showed that knockdown of *Pcm1* in cultured ependymal cells led to disrupted cilia ultrastructure and motility (Zhao et al., 2021).

To explore whether defects in ependymal cilia could be the cause of hydrocephaly in *Pcm1*<sup>-/-</sup> mice, we imaged ependymal cilia in lateral ventricle walls. *Pcm1*<sup>-/-</sup> mice exhibited

---

161 numerous ependymal cell abnormalities, including fewer ependymal cells with multiple basal  
162 bodies at P3 and P5 (**Figure 3A-C, Figure 3 - figure supplement 1A**). However, by P16,  
163 *Pcm1*<sup>-/-</sup> mice had caught up and displayed normal numbers of ependymal cells with multiple  
164 basal bodies (**Figure 3C, Figure 3 - figure supplement 1B**). These results suggest a delay  
165 in centriole biogenesis in the absence of PCM1. Once committed as making multiple  
166 centrioles, the numbers of basal bodies per cell formed by *Pcm1*<sup>-/-</sup> ependymal cells *in vivo*  
167 was similar to controls at P5 (**Figure 3B, E**). However at this early stage, *Pcm1*<sup>-/-</sup> mice also  
168 exhibited increased numbers of cells with rosette-like arrangements of basal bodies (**Figure**  
169 **3B, F**). As rosettes are typically present earlier in ependymal centriole biogenesis, these  
170 results are consistent with the absence of PCM1 causing a delay in centriole biogenesis. In  
171 addition, basal bodies of *Pcm1*<sup>-/-</sup> ependymal cells displayed disrupted translational polarity of  
172 basal bodies within the apical domain, which persisted until P16 (**Figure 3B, G, H, Figure 3**  
173 **- figure supplement 1A, B**). Basal body positioning within the apical domain is thought to  
174 be independent of ciliary motility, suggesting roles for PCM1 in ependymal cells beyond  
175 motility (Kishimoto and Sawamoto, 2012; Mirzadeh et al., 2010b). Interestingly, *Pcm1*<sup>-/-</sup>  
176 ependymal cells contained highly elongated FOP- and Centrin-containing centriole-like  
177 structures measuring  $5.0 \pm 1.9 \mu\text{m}$  (mean  $\pm$  SD) in length (**Figure 3 - figure supplement**  
178 **2A-F**). Together these results suggest disrupted centriole biogenesis and migration in the  
179 absence of PCM1.

180         At P5, there were fewer *Pcm1*<sup>-/-</sup> ciliated ependymal cells, however by P16 the  
181 number of ciliated *Pcm1*<sup>-/-</sup> ependymal cells was equivalent to control ventricles (**Figure 3A,**  
182 **B, D, Figure 3 - figure supplement 1A, B**). This suggests a delay in ependymal  
183 ciliogenesis in the absence of PCM1, perhaps secondary to the delay in centriole  
184 biogenesis. At P3, *Pcm1*<sup>-/-</sup> ependymal cilia displayed ultrastructural defects, including  
185 missing microtubule doublets and fused axonemes (**Figure 3I, K**).

186         To further analyze the function of PCM1 in multiciliogenesis, we cultured primary  
187 ependymal cells (Guirao et al., 2010) isolated from P0-P3 wild-type control and *Pcm1*<sup>-/-</sup> mice.  
188 These *Pcm1*<sup>-/-</sup> ependymal cells possessed fewer centrioles at the disengagement stage of  
189 centriole biogenesis, but once the cells became multiciliated had normal numbers of  
190 centrioles (**Figure 3 - figure supplement 1C, E, G**). In culture, *Pcm1*<sup>-/-</sup> ependymal cells  
191 formed fewer cilia than control ependymal cells (**Figure 3J, L, Figure 3 - figure supplement**  
192 **1C, F**). High speed video microscopy revealed that *Pcm1*<sup>-/-</sup> ependymal cilia beat slowly and  
193 uncoordinatedly (**Figure 3J, M, N, Figure 3 - videos 1-3**). These findings further support  
194 the conclusion that the lack of PCM1 causes a delay in centriole biogenesis and disrupted  
195 motile ciliary function.

---

196 Thus, PCM1 is not essential for ciliogenesis, but is required for timely basal body  
197 biogenesis, maturation, migration and ciliogenesis in ependymal cells. We propose that  
198 hydrocephaly in *Pcm1*<sup>-/-</sup> mice is caused by delayed ependymal cell ciliogenesis and  
199 compromised ciliary motility.

200 Like the brain ventricles, the trachea is lined by motile multiciliated cells. To examine  
201 whether PCM1 also promotes ciliogenesis and ciliary motility in the airways, we examined  
202 mouse tracheal basal bodies and cilia by immunofluorescence. *Pcm1*<sup>-/-</sup> tracheal multiciliated  
203 cells *in vivo* did not display decreased numbers of basal bodies or cilia at P5, or altered  
204 axonemal ultrastructure at 6 months of age (**Figure 3- figure supplement 3B, C, D**). High  
205 speed video microscopy revealed *Pcm1*<sup>-/-</sup> tracheal cilia beat at normal frequency (**Figure 3 -**  
206 **figure supplement 3E, Figure 3 - videos 4 and 5**).

207 To investigate the dynamics of ciliogenesis in these cells, we differentiated mouse  
208 tracheal epithelial cells (mTECS) into multiciliated cells *in vitro* (Eenjes et al., 2018; You et  
209 al., 2002). Concurring with a previous reports on the dispensability of PCM1 in mTECs  
210 (Vladar and Stearns, 2007), *Pcm1*<sup>-/-</sup> mTECs displayed normal basal body biogenesis,  
211 ciliogenesis and ciliary beat frequency (**Figure 3 - figure supplement 3A, F**). However,  
212 proteomic analysis of differentiating *Pcm1*<sup>-/-</sup> mTECs revealed that many motile ciliary  
213 proteins, including dynein motors, dynein assembly factors and dynein docking factors, were  
214 reduced early in ciliogenesis (ALI day 7) (**Figure 3 - figure supplement 3G,**  
215 **Supplementary File 5**). Similar to the transitory delay we observed in *Pcm1*<sup>-/-</sup> ependymal  
216 cell ciliogenesis, proteomic differences in *Pcm1*<sup>-/-</sup> mTECs resolved by ALI day 21 (**Figure 3 -**  
217 **figure supplement 3G, Supplementary File 5**). Thus, as in ependymal cells, PCM1  
218 promotes timely cilia maturation in tracheal cells.

219 In multiciliated cells, PCM1 and other centriolar satellite proteins including CEP131  
220 and PCNT localize to fibrogranular material, satellite-like networks (Zhao et al., 2021).  
221 Consistent with previous findings from Zhao et al., we found that CEP131 in mTECs lacking  
222 PCM1 localized not to fibrogranular material but to centrioles, (**Figure 3O**). Similarly, in  
223 *Pcm1*<sup>-/-</sup> ependymal cells, CEP131 mislocalised to the centrioles, although rather than being  
224 absent from the fibrogranular material, this non-centriolar CEP131 pool became more  
225 elongated (**Figure 3 – figure supplement 1H**). Not all centriolar satellite components  
226 behaved similarly in the absence of PCM1; localization of PCNT was normal in *Pcm1*<sup>-/-</sup>  
227 ependymal cells (**Figure 3 – figure supplement 1I**). Thus, fibrogranular material in the  
228 absence of PCM1 can either be disrupted or change its distribution in different multiciliated  
229 cell types. Together, these results suggest that PCM1 is required for fibrogranular material  
230 integrity, centriole biogenesis and migration, and timely ciliogenesis in multiciliated cells.

---

**PCM1 is required for centriolar satellite integrity.**

To assess whether PCM1 is essential for centriolar satellite integrity, we analyzed *Pcm1*<sup>-/-</sup> MEFs and *PCM1*<sup>-/-</sup> RPE1 cells (Kumar et al., 2021). Immunoblot and immunofluorescence analyses confirmed loss of PCM1 protein in the mutant cells (**Figure 1A, B, Figure 4A, H**). In addition to PCM1 and CEP131, centriolar satellites contain proteins such as CEP290 and the E3 ligase MIB1 (Hall et al., 2013; Staples et al., 2012; Villumsen et al., 2013). In control RPE1 cells, CEP131 and CEP290 localized to both centriolar satellites and to the centrioles themselves. In *PCM1*<sup>-/-</sup> RPE1 cells, the centriolar satellite pool of CEP131 was absent, CEP290 was reduced and dispersed, and both displayed increased accumulation at centrioles (**Figure 4B, C**). In control MEFs, CEP131 and MIB1 localized to both centriolar satellites and to the centrioles themselves. In *Pcm1*<sup>-/-</sup> MEFs, the centriolar satellite pool of CEP131 was absent and MIB1 was reduced and dispersed, with CEP131 displaying increased accumulation at centrioles, similar to *Pcm1*<sup>-/-</sup> tracheal epithelial cells (**Figure 4D-G**). We conclude that PCM1 is critical for centriolar satellite integrity. In the absence of satellites, some satellite proteins (e.g., CEP131, CEP290) over-accumulate at centrioles, while others (e.g., MIB1) do not, highlighting the protein-specific role centriolar satellites play in controlling centriolar localization. We propose that centriolar satellites both deliver and remove select cargos from centrioles.

One way in which satellites could traffic cargos to and from centrioles would be via their movement within the cell. To visualize PCM1, we engineered mice expressing a fusion of PCM1 and the SNAP tag (Keppler et al., 2003) from the *Pcm1* locus. We derived MEFs from *Pcm1*<sup>SNAP</sup> mice, covalently labeled PCM1-SNAP with tetramethylrhodamine (TMR) (Crivat and Taraska, 2012), and imaged centriolar satellite movement relative to cilia. Consistent with previous reports (Conkar et al., 2019), centriolar satellites moved both towards and away from the ciliary base, with frequent fission and fusion at the ciliary base (**Figure 4 – video 1**).

To further explore how centriolar satellites promote ciliogenesis, we examined ciliogenesis in MEFs and RPE1 cells lacking PCM1. In accordance with previous observations (Odabasi et al., 2019; Wang et al., 2016), ciliogenesis was abrogated in several *PCM1*<sup>-/-</sup> RPE1 cell lines (**Figure 4H - J**) and could be rescued by expression of eYFP-PCM1 (**Figure 4L**).

In marked contrast, and consistent with the tissue-specific effects of loss of PCM1 on ciliogenesis (**Figure 1 – figure supplement 3**), ciliogenesis was not perturbed in *Pcm1*<sup>-/-</sup> MEFs, with *Pcm1*<sup>-/-</sup> MEFs displaying cilia number, centrosome number and cilia length

---

indistinguishable from those of controls (**Figure 4K, M, Figure 4 - figure supplement 1A-D**). Thus, PCM1, despite broad roles in regulating the centriolar localization of proteins such as CEP131, plays cell-type specific roles in ciliogenesis.

#### **PCM1 is dispensable for removal of Centrobin and assembly of distal and sub-distal appendages.**

An early step in ciliogenesis is the removal of daughter centriole-specific protein Centrobins (Stephen et al., 2015; Wang et al., 2018). A previous study proposed a role for PCM1-localizing centriolar satellites in regulating the abundance of Talpid3, a component of the distal centriole implicated in the removal of Centrobins from the mother centriole (Wang et al., 2018, 2016). We found that both Talpid3 and Centrobins localization to centrioles in *PCM1*<sup>-/-</sup> RPE1 cells was equivalent to those of controls (**Figure 5 - figure supplement 1A - E**). Thus, Talpid3 recruitment to centrioles and Centrobins removal from the mother centriole are not dependent upon PCM1 or, by extension, centriolar satellites.

Distal appendages anchor the mother centriole to the ciliary membrane and sub-distal appendages position the cilium within cells (Mazo et al., 2016; Schmidt et al., 2012; Sillibourne et al., 2013; Tanos et al., 2013). Since centriolar satellite cargos (e.g., CEP90, OFD1 and MNR) are essential for ciliogenesis and distal appendage assembly (Kumar et al., 2021), we hypothesized that PCM1 may participate in distal or sub-distal appendage formation. To test this hypothesis, we examined localization of components of the distal (i.e., FBF1 and ANKRD26) and sub-distal appendages (i.e., Ninein) at the mother centriole. In *PCM1*<sup>-/-</sup> RPE1 cells, both distal and sub-distal appendage components localized to the mother centriole (**Figure 5 - figure supplement 1F-K**), although the amount of distal appendage proteins at the mother centriole was slightly reduced. Serial section transmission electron microscopy (TEM) confirmed that sub-distal and distal appendages were present in *PCM1*<sup>-/-</sup> RPE1 cells (**Figure 5 - figure supplement 2**). Therefore, centriolar satellites are not required for the assembly of distal or sub-distal appendages at the mother centriole.

#### **PCM1 promotes formation of the ciliary vesicle.**

After acquiring distal appendages, the mother centriole docks to preciliary vesicles, small vesicles which accumulate at the distal appendages of the mother centriole and are converted into a larger ciliary vesicle (Schmidt et al., 2012; Sillibourne et al., 2013; Tanos et al., 2013). To further examine the cause of reduced ciliogenesis in RPE1 cells lacking

---

centriolar satellites, we investigated whether preciliary vesicle docking or ciliary vesicle formation depends on PCM1.

Myosin-Va adorns preciliary and ciliary vesicles (Wu et al., 2018). Using 3D-SIM imaging of Myosin-Va, we identified preciliary vesicles at the basal bodies of control RPE1 cells soon after the induction of ciliogenesis (i.e., after 1 h of serum starvation). *PCM1*<sup>-/-</sup> RPE1 cells showed reduced Myosin-Va at preciliary vesicles (**Figure 5A, B**), suggesting that centriolar satellites promote timely docking of preciliary vesicles.

Since Myosin-Va marks both preciliary and ciliary vesicles, we more specifically assessed ciliary vesicle formation at the mother centriole by examining the localization of RAB34. RAB34 is a GTPase that marks the ciliary vesicle early in ciliogenesis and the ciliary sheath later (Ganga et al., 2021). Using 3D-SIM imaging, we observed RAB34 at the centrosome of wild-type RPE1 cells after 1 h serum starvation, and at both centrosomes and ciliary sheaths after 24 h serum starvation (**Figure 5C, D**). *PCM1*<sup>-/-</sup> RPE1 cells showed reduced RAB34 at both centrosomes and ciliary sheaths (**Figure 5C, D**), suggesting that centriolar satellites promote timely docking of the mother centriole to the preciliary vesicles, and the fusion of preciliary vesicles into a ciliary vesicle.

To assess ciliary vesicle formation using a complementary approach, we performed serial section TEM of control and *PCM1*<sup>-/-</sup> RPE1 cells early in ciliogenesis (i.e., after 1 h of serum starvation). We quantified preciliary and ciliary vesicles at mother centrioles. In *PCM1*<sup>-/-</sup> cells, mother centrioles (identified by the presence of distal and sub-distal appendages) exhibited reduced association with preciliary and ciliary vesicles (**Figure 5E, F, Figure 5 - figure supplement 2**). Thus, centriolar satellites promote the attachment of the mother centriole to preciliary vesicles and formation of the ciliary vesicle, important early steps in ciliogenesis.

### **PCM1 promotes CP110 and CEP97 removal from the mother centriole.**

In vertebrates, CP110 is required for docking of the mother centriole to preciliary vesicles (Walentek et al., 2016; Yadav et al., 2016) and is removed from the mother centriole subsequent to formation of the ciliary vesicle (Lu et al., 2015; Wu et al., 2018). The cap comprised of CP110 and CEP97 inhibits ciliogenesis, and its removal from the distal mother centriole is important for axoneme elongation (Spektor et al., 2007; Yadav et al., 2016). Since PCM1 promotes timely ciliary vesicle formation, we examined whether CP110 and CEP97 removal also depends on PCM1. In contrast to control cells, CP110 and CEP97

---

332 persisted at the distal mother centriole in *PCM1*<sup>-/-</sup> RPE1 cells after 24 hours of serum  
333 starvation (**Figure 6A-D**).

334 Interestingly, in wild-type MEFs, a small amount of CP110 persisted on the mother  
335 centriole even after axoneme formation (**Figure 6E, G-H**). Strikingly, mother centrioles in  
336 *Pcm1*<sup>-/-</sup> MEFs had CP110 levels comparable to daughter centrioles after 24 h serum  
337 starvation, despite undergoing ciliogenesis at rates equal to that of wild-type cells (**Figure**  
338 **6E, G-H**). Thus, PCM1 is essential for removing CP110 from the mother centriole, but  
339 CP110 removal is not required for ciliogenesis in MEFs.

340 Similar to RPE1 cells and MEFs, in *Pcm1*<sup>-/-</sup> ependymal cells *in vivo*, CP110 levels  
341 were elevated at P3, an age when ependymal cells are engaged in ciliogenesis (**Figure 6F,**  
342 **I**). Moreover, CP110 levels were elevated at the multiple basal bodies of *Pcm1*<sup>-/-</sup> tracheal  
343 multiciliated cells (**Figure 6 - figure supplement 1**). Thus, diverse cell types require PCM1  
344 to remove CP110 from the mother centriole, despite differentially requiring PCM1 for  
345 ciliogenesis.

#### 346 347 **PCM1 promotes transition zone formation and IFT recruitment.**

348 Following ciliary vesicle docking and removal of CP110 and CEP97 from the mother  
349 centriole, ciliogenesis proceeds with transition zone construction and IFT recruitment  
350 (Ishikawa and Marshall, 2011). Since PCM1 promotes ciliary vesicle docking and CP110 and  
351 CEP97 removal, we hypothesized that, in cells lacking PCM1, the subsequent engagement  
352 of IFT and transition zone components would be compromised.

353 To test this hypothesis, we immunostained control and *PCM1*<sup>-/-</sup> RPE1 cells with  
354 antibodies to IFT88 and IFT81. As expected, IFT88 and IFT81 localized to mother centrioles  
355 and along the length of cilia in control cells (**Figure 7A, C**). Localization of both IFT88 and  
356 IFT81 at mother centrioles was reduced in *PCM1*<sup>-/-</sup> RPE1 cells (**Figure 7A-D**), suggesting  
357 that IFT recruitment to the mother centriole is promoted by centriolar satellites. In contrast,  
358 ciliary and basal body levels of IFT88 were normal in *Pcm1*<sup>-/-</sup> MEFs (**Figure 7- figure**  
359 **supplement 1A, B**), indicating a concordance between PCM1-dependent IFT recruitment  
360 and ciliogenesis.

361 The transition zone controls ciliary protein composition. We determined whether  
362 PCM1 was required for the formation of the transition zone by assessing the localization of  
363 CEP162, an axoneme-associated protein that recruits components of the transition zone,  
364 such as RPGRIP1L (W.-J. Wang et al., 2013). Recruitment of CEP162 to the mother  
365 centriole was unaffected in *PCM1*<sup>-/-</sup> RPE1 cells (**Figure 7E, F**). In contrast, *PCM1*<sup>-/-</sup> RPE1

---

cells exhibited reduced RPGRIP1L at the transition zone (**Figure 7G, H**). Therefore, centriolar satellites promote both IFT recruitment and transition zone formation at RPE1 cell mother centrioles.

### **Centriolar satellites restrict CP110 and CEP97 levels at centrioles**

To explore the mechanisms by which centriolar satellites regulate CP110 and CEP97 levels at the centrioles, we examined the localization of TTBK2. TTBK2 is a kinase recruited by CEP164, a distal appendage component required to remove CP110 and CEP97 from mother centrioles (Goetz et al., 2012). In *PCM1*<sup>-/-</sup> RPE1 cells, TTBK2 recruitment to distal mother centrioles was equivalent to that of control cells (**Figure 7I, J**). These results suggest that centriolar satellites regulate CP110 and CEP97 removal from the distal mother centriole through a mechanism independent of TTBK2 recruitment.

As PCM1 is dispensable for the localization of TTBK2 at the distal mother centriole, we considered alternative mechanisms by which PCM1 may regulate local CP110 and CEP97 levels at the mother centriole. Since centriolar satellites are highly dynamic and localization of CP110 and CEP97 is actively controlled at the initiation of ciliogenesis, we hypothesized that CP110 and CEP97 are transported away from the centrioles via satellites. A prediction of this model is that CP110 and CEP97 should localize to satellites.

We examined RPE1 cells for CP110 and CEP97 and found that, indeed, CP110 and CEP97 colocalized with PCM1 and CEP290 at centriolar satellites in cycling cells (**Figure 8A, B, Figure 8 - figure supplement 1A, C**). Moreover, this satellite pool of CP110 was absent in *PCM1*<sup>-/-</sup> RPE cells (**Figure 8 - figure supplement 1B**). Consistent with CP110 and CEP97 co-localizing with PCM1 at centriolar satellites, CP110 and CEP97 co-immunoprecipitated with PCM1 in cycling cells (**Figure 8C**).

By examining RPE1 cells at different timepoints after serum depletion, we observed that the localization of CP110 and CEP97 to centrioles and centriolar satellites was dynamic: one hour after initiating ciliogenesis, CP110 and CEP97 at satellites decreased and, by 24 h of serum depletion, CP110 and CEP97 were absent from the mother centriole (**Figure 8A, B**).

CP110 interacts with satellite protein CEP290 (Tsang et al., 2008), so we hypothesized that CEP290 may hold CP110 at the satellites. Consistent with this model, CP110 no longer localized to satellites in cycling RPE1 cells upon *CEP290* knockdown (**Figure 8 - figure supplement 1D**). We propose that CP110 and CEP97 are centriolar satellite cargos which are wicked away from mother centrioles by centriolar satellites during early ciliogenesis.

---

401 If centriolar satellites transport CP110 and CEP97 away from centrioles as an early  
402 step in ciliogenesis, PCM1 may be critical for CP110 turnover. We therefore assessed total  
403 CP110 and CEP290 protein levels by immunoblot. In serum-starved *PCM1*<sup>-/-</sup> RPE1 cells,  
404 both CEP290 and CP110 were modestly elevated relative to serum-starved control cells  
405 (**Figure 8D, E**). Similarly, in synchronized RPE1 cells, CP110 levels were increased in the  
406 absence of PCM1, most markedly during mitosis and G0 (**Figure 8 - figure supplement**  
407 **1E**).

408 Where does this overabundant CP110 and CEP97 accumulate? Using  
409 immunofluorescence microscopy of cycling cells treated with nocodazole, we examined the  
410 localization of CP110 and CEP97 to centrioles. In the absence of PCM1, CP110 and CEP97  
411 over-accumulated at both centrioles (**Figure 8F-I**), suggesting that centriolar satellites  
412 restrict CP110 and CEP97 accumulation at centrioles.

413 We conclude that centriolar satellites restrict CP110 and CEP97 levels at centrioles,  
414 the removal of which promotes ciliogenesis in specific cell types. Centriolar satellites help  
415 promote timely ciliary vesicle formation and remove CP110 and CEP97 from the mother  
416 centriole, enabling recruitment of IFT and construction of the transition zone, early steps in  
417 ciliogenesis important for the prevention of ciliopathy-associated phenotypes such as  
418 hydrocephaly (**Figure 9**).

## 419 420 **Discussion**

### 421 **PCM1 performs select ciliogenic functions *in vivo*.**

422 Cilia are essential for key events in mammalian development; mice lacking cilia die  
423 during embryogenesis with developmental defects including randomized left-right axes and  
424 polydactyly (Ferrante et al., 2006; Huangfu et al., 2003). Many E18.5 *Pcm1*<sup>-/-</sup> tissues  
425 possessed cilia and *Pcm1*<sup>-/-</sup> mice survived at Mendelian ratios to birth and displayed no  
426 evidence of situs abnormalities or polydactyly, revealing that centriolar satellites are not  
427 required for mammalian ciliogenesis in many cell types.

428 Despite PCM1 being dispensable for ciliogenesis in many tissues, most *Pcm1*<sup>-/-</sup> mice  
429 died perinatally with hydrocephaly, delayed formation and disrupted function of ependymal  
430 cilia, oligospermia and abnormalities in tracheal epithelial cell ciliogenesis. In addition, *Pcm1*<sup>-/-</sup>  
431 mice exhibited cerebellar hypoplasia and partially penetrant hydronephrosis, both of which  
432 can be caused by defective Hedgehog signaling, a signal transduction pathway dependent  
433 on cilia (Huangfu et al., 2003; Spassky et al., 2008; Wallace, 1999; Wechsler-Reya and  
434 Scott, 1999; Yu et al., 2002). These phenotypes indicate that PCM1 promotes ciliogenesis in  
435 select cell types, many of which possess motile cilia.

---

436 Recently, a mouse *Pcm1* gene trap was described (Monroe et al., 2020). Aged mice  
437 homozygous for this allele exhibited enlarged brain ventricles, progressive neuronal cilia  
438 maintenance defects and late-onset behavioral changes, but not perinatal lethality or other  
439 early cilia-associated phenotypes. While background differences may influence penetrance  
440 and expressivity, it is possible that the absence of reported hydrocephaly and other  
441 ciliopathy-related phenotypes indicates that the *Pcm1* gene trap allele is hypomorphic.

442 Most human ciliopathies affect select tissues (Reiter and Leroux, 2017). For many  
443 ciliopathies, it remains unclear why tissues are differentially sensitive to ciliary defects. As  
444 mammalian PCM1 is particularly required for cilia function in ependymal cells and sperm,  
445 differential requirements for centriolar satellite function may be one determinant of tissue  
446 specificity in human ciliopathies.

#### 447 448 **PCM1 and centriolar satellites promote centriole amplification in ependymal cells.**

449 In almost all cells, centriole duplication is tightly restricted to make only two new  
450 centrioles per cell cycle (Nigg and Holland, 2018). In marked contrast, multiciliated cells  
451 produce tens to hundreds of centrioles. This centriole amplification has been proposed to  
452 occur by two mechanisms; (i) generation of new centrioles in proximity to the parental  
453 centrioles and (ii) generation via deuterosomes, electron dense structures unique to  
454 multiciliated cells (Mercey et al., 2019b; Nanjundappa et al., 2019; Zhao et al., 2013, 2019).  
455 However, centriole amplification and multiciliogenesis are not blocked in the absence of  
456 deuterosomes or parental centrioles (Mercey et al., 2019a, 2019b; Zhao et al., 2019),  
457 indicating that a third mechanism of centriole biogenesis exists.

458 A previous study demonstrated that knockdown of *Pcm1* in cultured mouse  
459 ependymal cells did not affect centriole number, but did alter ciliary structure (Zhao et al.,  
460 2021). We found that, in the absence of PCM1, ependymal cells displayed retarded centriole  
461 amplification and multiciliogenesis, as well as hydrocephaly. Our data indicate that PCM1,  
462 unlike deuterosomes, is critical for timely centriole amplification in ependymal cells. We  
463 propose that PCM1 is key to this previously postulated third mechanism of centriole  
464 amplification.

465 Ependymal cells lacking PCM1 also displayed disorganized beat patterns with  
466 disrupted basal body translational polarity. In contrast, tracheal multiciliated cells, which do  
467 not undergo clear planar polarization of basal body position, displayed normal beating in the  
468 absence of PCM1. We speculate that the role of PCM1 in basal body polarization could  
469 underlie its unique requirement for beat pattern in ependymal cells. Perhaps the involvement

---

of PCM1 in ependymal cell basal body polarization explains the presence of hydrocephaly in *Pcm1*<sup>-/-</sup> mice with no gross effect on airway mucus clearance.

*Pcm1*<sup>-/-</sup> ependymal cells also generated extremely long (3-7  $\mu$ m) centriole-like structures containing FOP and Centrin2. These centriole-related structures were present within the cytoplasm, distant from the apical domain where basal bodies nucleate cilia, and are reminiscent of elongated centrioles caused by depletion of CP110 (Spektor et al. 2007). One possibility is that the mechanisms by which CP110 and PCM1 restrain elongation are distinct. Alternatively, in multiciliated ependymal cells, the increased CP110 at many basal bodies may deplete the available CP110 pool, causing a minority of basal bodies to be depleted of CP110 and thereby elongate abnormally.

Consistent with prior observations by Zhao et al. (2021), *Pcm1*<sup>-/-</sup> tracheal and ependymal multiciliated cells showed altered fibrogranular material, intracellular networks to which many centriolar proteins localize. Interestingly, PCM1 loss affects fibrogranular material differently in ependymal cells and multiciliated tracheal cells: in *Pcm1*<sup>-/-</sup> mTECs, the fibrogranular material pool of CEP131 is absent and CEP131 accumulates at the basal bodies, whereas in *Pcm1*<sup>-/-</sup> ependymal cells, the fibrogranular material pool of CEP131 persists, but is altered, displaying a more fibrous organization. It is possible that by altering the fibrogranular material, the loss of PCM1 alters the distribution and function of centriolar proteins, resulting in delayed centriole biogenesis and the generation of long centriole-related structures.

#### **Centriolar satellites promote the timely removal of CP110 and CEP97 to support ciliogenesis**

Our work indicates that PCM1 and centriolar satellites help control the composition of centrioles. We found that in diverse cell types, including MEFs, RPE1, ependymal and tracheal cells, PCM1 promotes the removal of CP110 from distal mother centrioles, an early step in ciliogenesis. Similarly, PCM1 restricts levels of CEP131, CEP290 and CEP97 at centrioles. Recent work showed that *Pcm1* knockdown in ependymal cells also increased CEP135 and CEP120 localization to basal bodies (Zhao et al., 2021). Thus, centriolar satellites restrict the centriolar accumulation of multiple proteins.

A previous study proposed a role for PCM1 in protecting Talpid3 from degradation by sequestering the E3 ligase, MIB1 away from the centrioles (Wang et al., 2016). We found that, in the absence of PCM1, MIB1 no longer localizes to centrioles and Talpid3 levels on *PCM1*<sup>-/-</sup> centrioles were comparable to control centrioles, suggesting that PCM1 is not a critical determinant of centriolar Talpid3 levels. Talpid3 is required for distal appendage

---

assembly and removal of daughter centriole proteins (e.g., Centrobin) from mother centrioles (Wang et al., 2018). We found that PCM1 is dispensable for distal appendage assembly and removal of Centrobin from the mother centrioles, further suggesting that PCM1 and centriolar satellites are not required for Talpid3-dependent functions. Thus, centriolar satellites limit the centriolar localization of some, but not all, centriole components.

In the absence of PCM1, total cellular CP110 levels are increased and CP110 and CEP97 levels are elevated at centrioles, indicating a role for centriolar satellites in CP110 degradation. As CP110 and CEP97 transiently localized at satellites, we propose that satellites transport CP110 and CEP97 away from centrioles for degradation. Alternately, satellites could deliver proteins that degrade CP110 and CEP97 to the mother centriole. Such proteins could include UBR5, an E3 ubiquitin ligase that ubiquitylates CP110, the linear ubiquitin chain assembly complex (LUBAC) that also ubiquitylates CP110, or PRPF8, which removes ubiquitylated CP110 from centrioles (Gonçalves et al., 2021; Hossain et al., 2017; Shen et al., 2022). As centriolar satellite composition and distribution can change in response to environmental cues and stressors (Joachim et al., 2017; Prosser et al., 2022; Tollenaere et al., 2015; Villumsen et al., 2013), satellites likely help remove centriolar proteins beyond CP110 and CEP97.

The transient localization of CP110 to centriolar satellites is dependent on its interactor, CEP290. As inhibition of ciliogenesis by CP110 is dependent on CEP290 (Tsang et al., 2008), we suggest that one function for CEP290 may be to recruit CP110 to satellites for removal from mother centrioles.

In vertebrates, CP110 is required for docking of the mother centriole to preciliary vesicles (Walentek et al., 2016; Yadav et al., 2016) and is removed from the mother centriole subsequent to docking, suggesting that CP110 has both positive and inhibitory roles in ciliogenesis (Lu et al., 2015). Our finding that PCM1 promotes both CP110 removal and vesicular docking of the mother centriole suggests that centriolar satellites are involved in both intimately connected processes. One possibility is that centriolar satellites promote preciliary vesicle formation via transporting CP110 away from the mother centriole. This possibility is supported by data indicating that WDR8, another centriolar and centriolar satellite component, also contributes to CP110 removal from mother centrioles and ciliary vesicle formation (Kurtulmus et al., 2016). However, centriolar satellites may contribute to preciliary vesicle docking through mechanisms independent of CP110 removal. For example, although PCM1 is dispensable for distal appendage formation, the subtle changes in some distal appendage component localization in *PCM1*<sup>-/-</sup> cells could alter distal appendage composition or conformation in ways that compromise preciliary vesicle docking.

---

540 Interestingly, despite centriolar satellites promoting removal of CP110 from MEF  
541 mother centrioles, they are dispensable for ciliogenesis in MEFs. Therefore, removal of all  
542 CP110 from mother centrioles is not a precondition for ciliogenesis in some cell types.  
543 Multiple roles for CP110, both promoting and inhibiting ciliogenesis, have previously been  
544 described (Gonçalves et al., 2021; Spektor et al., 2007; Walentek et al., 2016; Yadav et al.,  
545 2016). One possible explanation for the cell-type specificity of PCM1 function is that  
546 centriolar satellites remove CP110 from mother centrioles in all cell types, but different  
547 thresholds of CP110 reduction are required to initiate ciliogenesis in different cell types.  
548 Thus, unlike core centriolar proteins, some of which are trafficked via centriolar satellites,  
549 centriolar satellites themselves are not essential for all centriole- and cilium-dependent  
550 events in many mammalian cell types.

551 These cell type-specific differences may reflect differences in how centrioles must be  
552 remodeled to effect duplication or ciliogenesis. Perhaps centriolar satellite-mediated CP110  
553 removal from mother centrioles is especially important for cells, like many epithelial cells, in  
554 which basal bodies dock directly to the plasma membrane, rather than to a ciliary vesicle. In  
555 the crowded environment at the heart of the centrosome, diffusion may be insufficient for the  
556 timely delivery and removal of centriolar proteins. PCM1 and centriolar satellites promote  
557 centriole amplification and ciliogenesis by coupling assembly and/or degradation of centriolar  
558 components in the satellites to their active transport to and from centrioles on microtubules.

559

---

## Acknowledgements

We thank the IGC Advanced Imaging Resource and the IGC Mass Spectrometry facility, as well as the Newcastle University Electron Microscopy Research services and, in particular, Tracey Davey. Work by the group of JFR is supported by NIH R01GM095941, R01AR054396 and R01HD089918. DK is supported by NIH K99 grant (5K99GM140175) and was funded by the Jane Coffin Childs memorial foundation and a Program for Biomedical Research award by the Sandler foundation. Work by the group of PM is supported by MRC intramural funding (MC\_UU\_12018/26) and by the European Commission (H2020 Grant No. 866355). Work by the group of LP is supported by CIHR Foundation (FDN#167279) and the Krembil Foundation. LP is a Tier 1 Canada Research Chair in Centrosome Biogenesis and Function and SLP was funded by a European Union Horizon 2020 Marie Skłodowska-Curie Global Fellowship (No. 702601).

## Declaration of Interests

The authors have declared no competing interests.

## Methods and Materials

### Generation of mouse models

Animals were maintained in SPF environment and studies carried out in accordance with the guidance issued by the Medical Research Council in “Responsibility in the Use of Animals in Medical Research” (July 1993) and licensed by the Home Office under the Animals (Scientific Procedures) Act 1986 under project license number P18921CDE in facilities at the University of Edinburgh (PEL 60/6025). *Pcm1* null mice (*Pcm1*<sup>Δ5-14/Δ5-14</sup>; *Pcm1*<sup>em1Pmi</sup> MGI:6865681 and *Pcm1*<sup>Δ796-800/Δ796-800</sup>; *Pcm1*<sup>em2Pmi</sup> MGI:6865682) were generated using CRISPR/Cas9 as described in **Figure 1 - figure supplement 1**, using guides detailed in **Supplementary File 1**. Genotyping was performed using primers detailed in **Supplementary File 2** followed by Sanger sequencing (for *Pcm1*<sup>Δ5-14/Δ5-14</sup>) or digestion with Ddel (for *Pcm1*<sup>Δ796-800/Δ796-800</sup>), or alternately genotyping was performed by Transnetyx. *Pcm1*<sup>SNAP</sup> animals were generated with CRISPR Cas9 targeting first coding exon 2 (**Supplementary File 1**) and a SNAP tag was inserted after the ATG, followed by a GSGG linker, using a repair template with 700 nt homology arms, detailed in **Supplementary File 1**, resulting in a gene encoding N-terminally SNAP tagged PCM1 in the endogenous locus. Genotyping was performed using primers detailed in **Supplementary File 2** or alternately by Transnetyx.

---

594

**595 Mouse gait analysis**

596 Gait analysis was performed on a Catwalk™ XT according to manufacturer's instructions.  
597 Briefly, mice were habituated to the Catwalk for 5 min, and then the glass was cleaned prior  
598 to acquisition. Each mouse (n>4 per experimental group) was then allowed to perform at  
599 least 3 runs across the Catwalk, which records paw position and analyses gait patterns  
600 using the Catwalk XT 10.6 Acquisition and Analysis Software.

601

**602 Retinal imaging**

603 Electroretinograms and fundal imaging was performed as described in (Findlay et al., 2018).  
604 PCM1-SNAP retinal labelling was carried out under inhaled anesthesia. 1.5 µl of 0.6 µM  
605 SNAP-Cell 647-SiR (New England Biolabs) was injected into the mouse vitreous under  
606 direct visualization using a Zeiss operating microscope. After 2 h, mice were sacrificed by  
607 cervical dislocation and eyes enucleated. Keratectomy, sclerectomy and lensectomy were  
608 performed and whole retinas isolated. Flat mount petaloid retinal explants were made and  
609 mounted, photoreceptor side up, on Menzel\_Glaser Superfrost Plus Gold slides  
610 (ThermoFisher Scientific; K5800AMNZ72). Nuclei were stained with DAPI and mounted in  
611 Prolong Gold under coverslip. Slices were imaged on an Andor Dragonfly spinning disc  
612 confocal.

613

**614 Cell lines and cell culture**

615 Mouse embryonic fibroblasts (MEFs) were maintained as previously published (Hall et al.,  
616 2013). SNAP labelling was performed as previously described (Quidwai et al., 2021).  
617 Ependymal cells were isolated and cultured as published in (Delgehyr et al., 2015). MTECs  
618 were isolated and cultured as described in (Eenjes et al., 2018; You et al., 2002). RPE1-  
619 hTERT (female, human epithelial cells immortalized with hTERT, Cat. No. CRL-4000) from  
620 ATCC were grown in DMEM (Life Technologies) or DMEM/F12 (ThermoFisher Scientific,  
621 10565042) supplemented with 10% FBS at 37°C with 5% CO<sub>2</sub>. For live imaging, the  
622 membrane was cut out and placed cilia down on a glass dish (Nest, 801002) in a drop of  
623 media. *PCM1*<sup>-/-</sup> RPE1 cells were generated as described previously (Kumar et al., 2021) (all  
624 figures except for **Figure 8 – figure supplement 1**, in which case they were generated as in  
625 (Gheiratmand et al., 2019)). hTERT-RPE1: Source ATCC, confirmed mycoplasma negative  
626 and verified by STR profiling. Two *PCM1*<sup>-/-</sup> RPE1 cell lines were generated using single  
627 guide RNAs (**Supplementary File 1**). Loss of PCM1 was confirmed by genotyping,  
628 immunoblotting, and immunofluorescence. Monoclonal *PCM1*<sup>-/-</sup> RPE1 cell lines stably  
629 expressing eGFP or eYFP-PCM1 (plasmid a gift from Bryan Dynlacht; (Wang et al., 2016))  
630 were generated using lentiviruses and manually selected based on fluorescence. To

---

synchronize cells in G1/S aphidicolin (Sigma) was added to the culture medium at 2 µg/ml for 16 h. To arrest cells in mitosis, taxol (paclitaxel; Millipore-Sigma) was added to the culture medium at 5 µM for 16 h prior to rounded up cells being collected by mitotic shake-off. For arrest in G0, cells were washed 2x with PBS (Gibco) and 1x with DMEM (without serum) before being cultured in serum-free DMEM for 16 h. To disrupt cytoplasmic microtubules, cells were treated with 20 µM nocodazole (Sigma, SML1665) for 1-2 h prior to fixation.

### **RNA-mediated interference**

hTERT RPE-1 cells were transfected with 20 nM (final concentration) of the respective siRNA for 48 h using Lipofectamine RNAiMAX (Invitrogen) according to the manufacturer's instructions. Effective knockdown was confirmed by immunofluorescence microscopy. Details of individual siRNAs are provided in the **Supplementary File 1**.

### **Proteomics**

MTECs were lysed in 0.1 % SDS in PBS plus 1X HALT protease inhibitor ThermoFisher Scientific, 78443), then processed by a multi-protease FASP protocol as described (Wiśniewski and Mann, 2012). In brief, SDS was removed and proteins were first digested with Lys-C (Wako) and subsequently with Trypsin (Promega) with an enzyme to protein ratio (1:50). 10 µg of Lys-C and Trypsin digests were loaded separately and desalted on C18 Stage tip and eluates were analyzed by HPLC coupled to a Q-Exactive mass spectrometer as described previously (Farrell et al., 2014). Peptides and proteins were identified and quantified with the MaxQuant software package, and label-free quantification was performed by MaxLFQ (Cox et al., 2014). The search included variable modifications for oxidation of methionine, protein N-terminal acetylation, and carbamidomethylation as fixed modification. Peptides with at least seven amino acids were considered for identification. The false discovery rate, determined by searching a reverse database, was set at 0.01 for both peptides and proteins. All bioinformatic analyses were performed with the Perseus software (Tyanova et al., 2016). Intensity values were log-normalized, 0-values were imputed by a normal distribution 1.8  $\pi$  down of the mean and with a width of 0.2  $\pi$ .

Proteomic expression data was analysed in R (3.6.0) with the Bioconductor package DEP (1.6.1) (Zhang et al., 2018). To aid in the imputation of missing values only those proteins that are identified in all replicates of at least one condition were retained for analysis. The filtered proteomic data was normalized by variance stabilizing transformation. Following normalization, data missing at random, such as proteins quantified in some replicates but not in others, were imputed using the k-nearest neighbour approach. For differential expression analysis between the wildtype and mutant groups, protein-wise linear

---

models combined with empirical Bayes statistics were run using the Bioconductor package limma (3.40.6) (Ritchie et al., 2015). Significantly differentially expressed proteins were defined by an FDR cutoff of 0.05. Total proteomic data are available via ProteomeXchange with identifier PXD031920 and are summarized in **Supplementary File 5**.

### **Immunoblotting**

Testes were lysed in RIPA buffer (Pierce) plus HALT protease inhibitor (ThermoFisher Scientific), homogenized with an electronic pestle for 1 minute, incubated at 4 °C with agitation for 30 min, sonicated for 3X 30 sec, and then clarified at 14,000 g at 4 °C for 20 min. RPE lysates were collected in 2x SDS-PAGE buffer and treated with benzonase nuclease (Millipore-Sigma) for 5 min. Samples were loaded into NuPAGE precast gels, transferred onto PVDF membrane (Amersham Hybond P, Cytiva), and then rinsed in water then TBST, and then blocked in 5% milk in TBS plus 0.1% Tween. Membranes were then incubated overnight at 4 °C in primary antibodies (**Supplementary File 3**) diluted in 5% milk TBST. Membranes were then washed 3 X 10 min TBST, incubated in HRP conjugated secondary antibodies detailed in **Supplementary File 4** for 1 h at room temperature and developed using Pierce SuperSignal Pico Plus (Pierce) or ECL (GE Healthcare) reagent and imaged on ImageQuant.

### **Co-immunoprecipitation**

Co-immunoprecipitation assays and western blots were performed as described previously (Kumar et al., 2021) using GFP trap magnetic agarose beads (Chromotek, gtma-10).

### **Ventricle and tracheal wholemount**

Ventricles were dissected according to (Mirzadeh et al., 2010a), pre-extracted with 0.1% Triton X in PBS for 1 minute, then fixed in 4% PFA or ice cold methanol for at least 24 h at 4 °C, followed by permeabilization in PBST (0.5% Triton X-100) for 20 min room temperature. Tracheas were dissected and cut longitudinally into two, pre-extracted in for 30 sec on ice in PEM (0.1 M PIPES pH 6.8, 2 mM EGTA, 1 mM MgSO<sub>4</sub>) prior to fixing in ice cold methanol on ice for at least 24 hours. Ventricles and tracheas were blocked in 10% donkey serum in TBST (0.1% Triton-X) or 4% BSA in PBST (0.25% Triton X-100) for one h at room temperature, then placed cilia layer down in primary antibodies (**Supplementary File 3**) in 4% BSA PBST (0.25% Tween-20) or 1% donkey serum in TBST (0.1% Triton-X) for at least 12 h. Ventricles and tracheas were washed in PBS 3 X 10 min and secondaries (**Supplementary File 4**) in 4% BSA in PBST (0.25% Triton X-100) or 1% donkey serum in TBST (0.1% Triton-X) were added at 4 °C for at least 12 h. Ventricles and tracheas were

---

washed in PBS 3 X 10 min, and ventricles were mounted on glass bottom dishes (Nest, 801002) in Vectashield (VectorLabs), immobilized with a cell strainer (Greiner Bio-One, 542040). Tracheas were mounted on slides with Prolong Gold.

## **Histology**

Kidneys and brains were fixed in 4% PFA/PBS, testes were fixed in Bouin's fixative, and eyes and E18.5 embryos were fixed in Davidson's fixative according to standard protocols. Tissues were serially dehydrated and embedded in paraffin. Microtome sections of 8  $\mu$ m thickness were examined histologically via haematoxylin and eosin (H&E) or periodic acid-Schiff (PAS) staining.

For immunofluorescent analysis, paraffin sections were dewaxed and re-hydrated via ethanol series, followed by antigen retrieval by boiling the sections for 15 min in the microwave in citrate buffer. Sections were blocked in 10% donkey serum/0.1% Triton-X100 in PBS and primary antibodies were diluted in 1% donkey serum/PBS (**Supplementary File 3**). Slides were washed and incubated in Alexafluor conjugated secondary antibodies (**Supplementary File 4**), washed and mounted in ProLong Gold (ThermoFisher Scientific).

## **Immunofluorescence**

MEFs, mTECs and cultured ependymal cells were processed for immunofluorescence as published (Hall et al., 2013). Briefly, cells were washed twice with warm PBS, then fixed in either 4% PFA in 1X PHEM/PBS 10 min at 37 °C, or pre-extracted for 30 sec on ice in PEM (0.1 M PIPES pH 6.8, 2 mM EGTA, 1 mM MgSO<sub>4</sub>) prior to fixing in ice cold methanol on ice for 10 min according to **Supplementary File 3**, then washed twice with PBS. Cells were permeabilized and blocked with 10% donkey serum in 0.1% Triton-X 100/TBS for 60 min at room temperature, or overnight at 4 °C. Primary antibodies (**Supplementary File 3**) were added to samples and incubated for 4 °C overnight, in dilutant made of 1% donkey serum in 0.1% Triton X-100/TBS. Samples were washed in 0.1% Triton-X 100/TBS 4-6 times, 10 min each. Secondary antibodies (**Supplementary File 4**) diluted in 1% donkey serum and 0.1 % Triton X-100/TBS were added for 60 min at room temperature, in some cases co-stained with AlexaFluor 647 Phalloidin (ThermoFisher Scientific), added with the secondaries at 1/500 for 1 h at room temperature. Samples were washed with 0.1% Triton-X 100/TBS 4-6 times 10 min, stained with DAPI (1:1000) in 0.1% Triton X-100/TBS for 5 min at room temperature, and mounted using ProLong Gold antifade (ThermoFisher Scientific), according to the manufacturer's instructions.

RPE1 cells were fixed with 100% cold methanol for 3 min and incubated in blocking buffer (2.5% bovine serum albumin (BSA), 0.1% Triton X-100 in PBS) for 1 h at room

---

temperature (except in **Figure 8 – figure supplement 1**, where they were fixed in ice cold methanol for 10 min and incubated in 2% BSA in PBS for 10 min at room temperature). Coverslips were then incubated in primary antibodies (**Supplementary File 3**) in blocking buffer overnight at 4°C or room temperature for 50 min, washed three times with PBS and incubated with secondary antibodies (**Supplementary File 4**) in blocking buffer for 1 h at room temperature along with Hoechst 33352 or DAPI (0.1 µg/ml). Coverslips were washed three times with PBS and mounted with Prolong Diamond (ThermoFisher Scientific P36961) or ProLong Gold Antifade (Molecular Probes). For TTBK2 staining, cells were fixed with 4% PFA/PBS for 10 min in general tubulin buffer (80 mM PIPES, pH 7, 1 mM MgCl<sub>2</sub>, and 1 mM EGTA), permeabilized with 0.1% TX-100 and stained as described above (Loukil et al., 2017).

### **Sperm preparation**

Cauda and caput epididymides were dissected into M2 media (ThermoFisher Scientific). For live imaging, sperm were imaged in M2 media or 1% methyl cellulose (Sigma), in capillary tubes (Vitrotubes Mountain Leaks) sealed with Cristaseal (Hawskley). Sperm counts were performed on sperm from the cauda epididymides, diluted in H<sub>2</sub>O using a haemocytometer, only counting intact sperm (with both head and tail).

### **Transmission electron microscopy**

Samples were dissected into PBS. Samples were fixed in 2% PFA/2.5% glutaraldehyde/0.1 M Sodium Cacodylate Buffer pH 7.4 (Electron Microscopy Sciences). Lateral ventricle walls were fixed for 18 h at 4 °C then subdissected into anterior, mid and posterior sections. Tissue was rinsed in 0.1 M sodium cacodylate buffer, post-fixed in 1% OsO<sub>4</sub> (Agar Scientific) for one h and dehydrated in sequential steps of acetone prior to impregnation in increasing concentrations of resin (TAAB Lab Equipment) in acetone followed by 100%, placed in moulds and polymerized at 60 °C for 24 h.

Ultrathin sections of 70 nm were subsequently cut using a diamond knife on a Leica EM UC7 ultramicrotome. Sections were stretched with chloroform to eliminate compression and mounted on Pioloform filmed copper grids prior to staining with 1% aqueous uranyl acetate and lead citrate (Leica). They were viewed on a Philips CM100 Compustage Transmission Electron Microscope with images collected using an AMT CCD camera (Deben).

RPE1 cells processed for TEM analysis were cultured on Permanox slides (Nunc 177445), serum starved for 1 h and processed as described previously (Kumar et al., 2021).

## Imaging

Brightfield images in **Figure 2** and **Figure 2 - figure supplement 1** were imaged on a Hamamatsu Nanozoomer XR with x20 and x40 objectives. Macroscopic images in **Figure 1** and **Figure 2** were imaged on a Nikon AZ100 Macroscopic. **Figure 1 – figure supplement 3** was imaged on Leica Stellaris DMI8 equipped with 4 (HyD X/HyD S) GaSP detectors with 40X or 60X oil objectives. Fluorescent images in **Figure 2, Figure 3A, Figure 3 - figure supplement 1A, B, Figure 3 - figure supplement 2A, Figure 3 - figure supplement 3 and Figure 7 - figure supplement 1** were taken on a Nikon A1+ Confocal with Oil 60 or 100x objectives with 405, Argon 561 and 640 lasers and GaSP detectors. Fluorescent images in **Figure 1, Figure 2 – figure supplement 1D, Figure 4D, E and K, Figure 4 - figure supplement 1, Figure 6 – figure supplement 1** were taken with Andor Dragonfly and Mosaic Spinning Disc confocal. Images in **Figure 3B and O, Figure 3 – figure supplement 1C, H, I, Figure 3 – figure supplement 2C-E and Figure 6E and F** were taken with Nikon SORA with 405 nm 120 mW, 488 nm 200 mW and 561nm 150mW lasers, 100x 1.35 NA Si Apochromat objective and a Photometrics Prime 95B 11mm pixel camera. High speed video microscopy was performed on a Nikon Ti microscope with a 60X Nikon Plan Apo VC 60X/1.20 water immersion objective, and Prime BSI, A19B204007 camera, imaged at 250 fps. 3D-SIM imaging in **Figure 4B, C, H, Figure 5, Figure 5 - figure supplement 1, Figure 6A, B, Figure 7 and Figure 8** was performed using the GE Healthcare DeltaVision OMX-SR microscope equipped with the 60x/1.42 NA oil-immersion objective and three CMOS cameras. Immersion oil with refractive index of 1.518 was used for most experiments, and z stacks of 5-6  $\mu\text{m}$  were collected every 0.125  $\mu\text{m}$ . Images were reconstructed using GE Healthcare SoftWorx 6.5.2 using default parameters. Images for quantifications were collected at the widefield setting using the same microscope. **Figure 8 – figure supplement 1** was imaged using a DeltaVision Elite high-resolution imaging system equipped with a sCMOS 2048 x 2048 pixel camera (GE Healthcare). Z-stacks (0.2  $\mu\text{m}$  step) were collected using a 60x 1.42 NA plan apochromat oil-immersion objective (Olympus) and deconvolved using softWoRx (v6.0, GE Healthcare).

## Image analysis

Image analysis was performed in NIS Elements, FIJI (Schindelin et al., 2012), QuPath (Bankhead et al., 2017), CellProfiler (Stirling et al., 2021) or Imaris. All analysis tools have been made available on GitHub ([https://github.com/IGC-Advanced-Imaging-Resource/Hall2022\\_Paper](https://github.com/IGC-Advanced-Imaging-Resource/Hall2022_Paper)). Cerebellum and ventricle area was measured from PAS stained sagittal brain sections in QuPath. The number of cilia in E18.5 ribs was calculated using Batch Pipeline in Imaris, segmenting DAPI and cilia as surfaces. The number of ependymal cells with multiple basal bodies was calculated by segmenting FOP staining and cells in 2D

using a CellProfiler pipeline. Briefly, an IdentifyPrimaryObjects module was used to detect the nuclei, followed by an IdentifySecondaryObjects module using the tubulin stain to detect the cell boundaries. Another Identify Primary objects module was used to detect the basal bodies and a RelateObjects module was used to assign parent-child relationships between the cells and basal bodies. The percentage of ciliated ependymal cells, and the number of ependymal cells with rosette-like FOP staining, and elongated FOP positive structures were counted by eye using NIS Elements Counts Tool. Analysis of cultured ependymal cells (beat frequency, number of cilia, coordinated beat pattern) and beat frequency determination in mTECs and trachea was assessed in FIJI by eye while blinded to genotype. The number of centrioles and cilia in cultured ependymal cells was manually calculated using Imaris. CEP131 and MIB1 intensity at satellites was calculated in FIJI using a macro which segmented basal bodies with Gamma Tubulin, then drew concentric rings, each 0.5  $\mu\text{m}$  wider than the previous and calculated the intensity of MIB1 and CEP131 within these rings. CP110 intensity in MEFs was calculated by manually defining mother and daughter centrioles in FIJI, CP110 intensity in ependyma and tracheas was calculated by segmenting FOP in 3D in Imaris and calculating CP110 intensity within this volume. Image quantification in RPE1 cells were performed using CellProfiler as described previously (Kumar et al., 2021). Images were prepared for publication using FIJI, Imaris, Adobe Photoshop, Illustrator and InDesign.

### Data analysis

Data analysis was carried out in Microsoft Excel, Graphpad Prism 6/9 and Matlab. Statistical tests are described in the Figure legends.

### Figure legends

**Figure 1. PCM1 is important for perinatal survival. (A)** Immunoblot of MEF lysates from wild-type and *Pcm1*<sup>-/-</sup> MEFs for PCM1 and GAPDH (loading control). Gel stained with Coomassie blue. **(B)** Immunostaining of PCM1 (yellow) and centrioles ( $\gamma$ -tubulin,  $\gamma$ -TUB, magenta) in wild-type MEFs and in *Pcm1*<sup>-/-</sup> MEFs. **(C)** E18.5 wild-type and *Pcm1*<sup>-/-</sup> neonates. **(D)** Kaplan-Meier curve of wild-type, *Pcm1*<sup>+/-</sup> and *Pcm1*<sup>-/-</sup> mice. See also **Figure 1 – figure supplement 1D. (E)** P28 wild-type, *Pcm1*<sup>+/-</sup> and *Pcm1*<sup>-/-</sup> mice. **(F)** Graph of body weights of wild-type, *Pcm1*<sup>+/-</sup> and *Pcm1*<sup>-/-</sup> mice by age. Student's t-test \*  $P < 0.05$ , \*\*  $P < 0.01$ , \*\*\*  $P < 0.001$ .

**Figure 1 - figure supplement 1. PCM1 promotes survival and growth.**

---

(A) Schematics of two CRISPR/Cas9-generated indels in *Pcm1*, *Pcm1*<sup>Δ5-14</sup> and *Pcm1*<sup>Δ796-800</sup>. Both *Pcm1*<sup>Δ5-14</sup> and *Pcm1*<sup>Δ796-800</sup> create frameshifts. Schematic of PCM1 protein, indicating predicted coiled-coil domains and epitopes used for generating anti-PCM1 antibodies. (B) Label-free quantitative (LFQ) mass spectrometry of PCM1 peptides in wild-type and *Pcm1*<sup>-/-</sup> mouse tracheal epithelium cells (mTECs) differentiated for seven days at air-liquid interface. Student's t-test \*\*\* P < 0.01. (C) Immunoblot of *Pcm1*<sup>Δ5-14/Δ5-14</sup> and *Pcm1*<sup>Δ796-800/Δ796-800</sup> testis lysates for PCM1 using antibody directed against the PCM1 N-terminus (N), C-terminus (C) and α-tubulin (loading control). (D) Number of *Pcm1*<sup>-/-</sup> animals genotyped at each age as a percentage of the expected number, \* P < 0.05, \*\*\* P < 0.001, Chi squared. n represents number of animals genotyped at given age. (E) E18.5 wild-type and *Pcm1*<sup>-/-</sup> embryo weights. Each pair of points represents the average control or *Pcm1*<sup>-/-</sup> embryo weight in a given litter. Paired t-test. \* P < 0.05, \*\*\* P < 0.001. (F) Wild-type and *Pcm1*<sup>-/-</sup> brain weights at various ages from P30-P270. (G) Wild-type and *Pcm1*<sup>-/-</sup> brain weights relative to body weight at various ages from P30-P270. ns: not significant. (F, G) Paired t-test, sex and litter matched. \*\* P < 0.01, ns: not significant. CTRL: control, combined wild-type and *Pcm1*<sup>+/-</sup> mouse measurements.

**Figure 1 - figure supplement 2. *Pcm1*<sup>Δ5-14/Δ5-14</sup> and *Pcm1*<sup>Δ796-800/Δ796-800</sup> mice exhibit comparable phenotypes.** (A, B) Observed number of wild-type, *Pcm1*<sup>+/-Δ5-14</sup>, *Pcm1*<sup>Δ5-14/Δ5-14</sup>, *Pcm1*<sup>+/-Δ796-800</sup> and *Pcm1*<sup>Δ796-800/Δ796-800</sup> mice as a percentage of the expected number. Chi squared: \*\*\* P < 0.01, \* P < 0.05. (C, D) Body weights of wild-type, *Pcm1*<sup>+/-Δ5-14</sup>, *Pcm1*<sup>Δ5-14/Δ5-14</sup>, *Pcm1*<sup>+/-Δ796-800</sup> and *Pcm1*<sup>Δ796-800/Δ796-800</sup> mice. Student's t-test: \*\* P < 0.01, \*\*\* P < 0.001. (E, F) Percentage of control (heterozygote and wild-type), *Pcm1*<sup>Δ5-14/Δ5-14</sup> and *Pcm1*<sup>Δ796-800/Δ796-800</sup> mice displaying overt hydrocephaly. Chi squared: \*\* P < 0.01, \*\*\* P < 0.001.

**Figure 1 - figure supplement 3. PCM1 is dispensable for ciliogenesis in some cell types.**

(A, C, E) Sagittal sections of wild-type and *Pcm1*<sup>-/-</sup> E18.5 embryos immunostained for cilia (polyglutamylated tubulin: TUB<sup>PolyE</sup>, magenta and ARL13B, yellow). Nuclear stain (DAPI) in blue. Insets depict higher magnification views of demarcated areas. Tissues shown are ribs (A), kidney (C) and trachea (E). Primary cilia are marked by white arrows. (B) Percentage of E18.5 rib wild-type and *Pcm1*<sup>-/-</sup> cells that are ciliated. (D) Length of cilia in E18.5 wild-type and *Pcm1*<sup>-/-</sup> cortical kidney epithelial cells. n = 2 animals/genotype represented by large symbols, small symbols represent individual field of view. Student's t-test. ns: not significant. Scale bars represent 30 μm in main panels (A and C), 20 μm (E), and 10 μm insets.

**Figure 1 – source data 1.** Full uncropped immunoblots for Figure 1A and Figure 1 - figure supplement 1C, labelled and unlabelled.

**Figure 2. *Pcm1*<sup>-/-</sup> mice display ciliopathy-associated phenotypes.** (A) *Pcm1*<sup>-/-</sup> mouse displaying a domed skull indicative of hydrocephaly. (B) Coronal sections of 5-week-old wild-type and *Pcm1*<sup>-/-</sup> brains. (C) Percentages of wild-type and *Pcm1*<sup>-/-</sup> mice exhibiting hydrocephaly (n = 22 *Pcm1*<sup>-/-</sup> mice, age 19 days - 3 months (with hydrocephaly) and 6 weeks – 1 year (without overt hydrocephaly), n = 35 age matched littermate controls). (D) Gross morphology of 8-month-old wild-type and *Pcm1*<sup>-/-</sup> brains. Cerebella are delineated with dotted lines. (E) Quantification of cerebellar area measured from sagittal sections of 2 to 8-month-old brains from *Pcm1*<sup>-/-</sup> mice without frank hydrocephaly, normalized to the mean of wild-type cerebellar area. N = 3. Each shape represents a different animal. Error bars indicate standard deviations. Student's t-test: \* P < 0.05. (F) Cresyl violet-stained sagittal sections of 8-month-old brains. Cerebella are indicated with arrows. \* Dilated ventricle. (G) Percentage of time spent by adult wild-type and *Pcm1*<sup>-/-</sup> mice in alternate (AB) gait and cruciate (CA) gait. Mean +/- SEM. *Pcm1*<sup>+/+</sup> n = 4, *Pcm1*<sup>-/-</sup> n = 5. Student's t-test: \* P < 0.05. (H) H&E-stained sections of kidneys and adrenals from 6-week-old wild-type and *Pcm1*<sup>-/-</sup> mice. (I) Sperm count per ml of wild-type and *Pcm1*<sup>-/-</sup> epididymal semen. n = 3 per genotype. (J) PAS-stained sections of 3-month-old wild-type and *Pcm1*<sup>-/-</sup> seminiferous tubules. Insets are higher magnification images of elongated spermatids (see **Figure 2 supplement 1C** for lower magnification images), with a cartoon of sperm head morphology. (K) Immunofluorescence staining of wild-type and *Pcm1*<sup>-/-</sup> seminiferous tubules for sperm flagella (acetylated tubulin, TUB<sup>Ac</sup>, magenta) and nuclei (DAPI, blue). Scale bars represent 1 mm in B, 2.5 mm in F and H, 100 µm in J, and 50 µm in K.

**Figure 2 - figure supplement 1. *Pcm1*<sup>-/-</sup> mice display a subset of ciliopathy-associated phenotypes.** (A) Coronal (6-week, top images) and sagittal (8-month, bottom images) optical projection tomography (OPT) images of brains of wild-type and *Pcm1*<sup>-/-</sup> mice. Dilated ventricle is marked by an arrow. Cerebellar limits are indicated by arrowheads. Scale bar represents 1 mm. (B) Ventricle size relative to cortex size of wild-type and *Pcm1*<sup>-/-</sup> mice without overt hydrocephaly. Each point depicts a measurement from an individual sagittal section. Each shade represents a separate animal. Student's t-test: \* P < 0.05. (C) PAS staining of stage-matched wild-type and *Pcm1*<sup>-/-</sup> testis seminiferous tubules. Insets show enlargements of developing spermatids, with cartoons depicting spermatid morphology and stage number. Scale bar represents 50 µm in main panels and 10 µm in insets. (D) Intravitreal injection of TMR-SNAP into wild-type and *Pcm1*<sup>SNAP/SNAP</sup> eyes labels PCM1-SNAP in the retinas. DAPI marks nuclei (blue). Displayed is a single X-Z slice from a

confocal z stack. Scale bar represents 40  $\mu\text{m}$ . (E) Fundal imaging of 1-year-old wild-type and *Pcm1*<sup>-/-</sup> eyes. (F) H&E-stained sections of 13-month-old wild-type and *Pcm1*<sup>-/-</sup> retinas. Scale bar represents 20  $\mu\text{m}$ . (G) Electroretinograms (ERGs) of 9-month-old wild-type and *Pcm1*<sup>-/-</sup> mice. (H) Quantification of ERG A-waves, reflecting the rapid cornea negative potential. Student's t-test. (I). Quantification of ERG B-waves, reflecting the slow cornea positive potential. Student's t-test, ns = not significant.

**Figure 2 – video 1. Wild-type sperm morphology and movement.** Sperm were isolated from wild-type testes and imaged in dilute methyl cellulose.

**Figure 2 – video 2. *Pcm1*<sup>-/-</sup> sperm are immotile and lack normal head structures.** Sperm were isolated from *Pcm1*<sup>-/-</sup> testes and imaged in dilute methyl cellulose.

**Figure 2 – video 3. *Pcm1*<sup>-/-</sup> sperm exhibit disrupted movement.** Sperm were isolated from *Pcm1*<sup>-/-</sup> testes and imaged in media without methyl cellulose.

**Figure 3. PCM1 is required for efficient basal body synthesis and multiciliogenesis.**

(A) Wild-type and *Pcm1*<sup>-/-</sup> P3 wholemount brain ventricles immunostained for basal bodies (FOP, yellow), actin (phalloidin, cyan) and cilia (TUB<sup>Ac</sup>, magenta). Inset depicts area of ventricle imaged (cyan box). (B) Wild-type and *Pcm1*<sup>-/-</sup> P5 wholemount ventricles immunostained for basal bodies (FOP, yellow), cilia (TUB<sup>Ac</sup>, magenta), and nuclei (DAPI, blue). Below: single optical planes highlight the persistence of rosettes and disrupted ciliogenesis in *Pcm1*<sup>-/-</sup> ependymal cells. (C) Percentage of ependymal cells with >4 basal bodies in wild-type and *Pcm1*<sup>-/-</sup> P3, P5 and P16 ventricles. Each shape represents an animal; the smaller symbols represent individual images and the larger shape the mean for each animal. Student's t-test: \*  $P < 0.05$ , \*\*  $P < 0.01$ , ns: not significant. (D) Percentage of ependymal cells with multiple cilia in wild-type and *Pcm1*<sup>-/-</sup> P3, P5 and P16 ventricles. Student's t-test: \*\*\*  $P < 0.001$ , ns, not significant. (E) The number of basal bodies per wild-type and *Pcm1*<sup>-/-</sup> P5 ependymal cell. (F) Percentage of P3 wild-type and *Pcm1*<sup>-/-</sup> ependymal cells with centriolar rosette structures. Student's t-test: \*  $P < 0.05$ . (G, H) Rose plots of the translational polarity of basal bodies in wild-type and *Pcm1*<sup>-/-</sup> P5 and P16 ependymal cells, as assessed from immunofluorescent images as in **Figure 3 - figure supplement 1A and B**. Schematic insets represent individual ependymal cells with polarised or unpolarised basal bodies (yellow). An arrow was drawn from the center of the nucleus (blue) to the centre of the basal bodies (yellow) and the distance and angle is plotted relative to the average angle for that field of view, which was set to 0°. At both P5 and P16, the standard deviations

between wild-type and *Pcm1*<sup>-/-</sup> ependymal cells are different (F-test: \*\*\*  $P < 0.0001$ ). (I) TEM of ependymal cell cilia from P3 wild-type and *Pcm1*<sup>-/-</sup> ventricles. Wild-type cilia display 9+2 microtubule arrangement. *Pcm1*<sup>-/-</sup> cilia display axonemal defects, including missing microtubule doublets and axoneme fusion (indicated by \*). (J) Colourized heat map (scale: yellow - high, blue - low) of maximum projection of the standard deviation of pixel intensity in **Figure 3 - videos 1 and 2**, depicting wild-type and *Pcm1*<sup>-/-</sup> cultured ependymal cell cilia beat coordination. Areas of high pixel intensity variation reflect areas of increased movement. (K) Percentage of P3 wild-type and *Pcm1*<sup>-/-</sup> ependymal cilia structural anomalies. Chi squared test: \*\*\*  $P < 0.001$ .  $n = 121$  cilia from 3 wild-type mice and 61 cilia from 3 *Pcm1*<sup>-/-</sup> mice. (L) Percentage of cultured wild-type and *Pcm1*<sup>-/-</sup> ependymal cells with ranges of cilia number 14-16 days after serum withdrawal. Chi squared test: \*\*\*  $P < 0.001$ . ns: not significant. (M) Percentage of cultured wild-type and *Pcm1*<sup>-/-</sup> ependymal cells with coordinated ciliary beating 14-16 days after serum withdrawal. Chi squared test: \*\*\*  $P < 0.01$ . (N) Cilia beat frequency of cultured wild-type and *Pcm1*<sup>-/-</sup> ependymal cells 14-16 days after serum withdrawal. Small symbols represent individual cells, large symbols represent average for each cell lines from an individual animal. Student's t-test: \*\*\*  $P < 0.001$ , \*\*  $P < 0.01$ . (O) Representative images of wild-type and *Pcm1*<sup>-/-</sup> mTECs cultured at air-liquid interface for 3 days and immunostained for basal bodies (FOP, yellow) and CEP131 (magenta). Representative cells cultured from  $n = 3$  wild type and 3 *Pcm1*<sup>-/-</sup> animals, at the "centriolar amplification" (C/A), "growth" (G) and "disengagement" (D) stages of centriolar amplification are shown (see also **Figure 3 - figure supplement 1G**). Scale bars: 15  $\mu\text{m}$  (A), 5  $\mu\text{m}$  (B), 100 nm (I) and 1  $\mu\text{m}$  main panel, 2  $\mu\text{m}$  inset (O).

**Figure 3 - figure supplement 1. Centriole amplification is delayed and fibrogranular material is disrupted in *Pcm1*<sup>-/-</sup> ependymal cells.** (A, B) Ependymal cells from P5 (A) and P16 (B) wild-type and *Pcm1*<sup>-/-</sup> ventricles immunostained for basal bodies (FOP, yellow), cilia (TUB<sup>A</sup><sub>c</sub>, magenta) and, at P5, actin (phalloidin, cyan). (C) Cultured wild-type and *Pcm1*<sup>-/-</sup> ependymal cells three days after serum withdrawal and immunostained for basal bodies (FOP, yellow) and cilia (TUB<sup>A</sup><sub>c</sub>, magenta), at the "amplification" (A), "growth" (G), "disengagement" (D) and multiciliated cell (MCC) stages of centriolar amplification. (D) Percentage of wild-type and *Pcm1*<sup>-/-</sup> cultured ependymal cells at each stage of centriole amplification after 3 days of serum starvation. (E) The number of centrioles per ependymal cell at each stage of centriole amplification after 3 days of serum starvation. (F) The number of cilia per ependymal cell at each stage of centriole amplification after 3 days of serum starvation. For (D-F), each point represents a cell,  $n = 3$  cultures/genotype, each from a different mouse. 2-way ANOVA, Sidak corrected for multiple testing: ns, not significant, \*\*  $P < 0.01$ . (G) Schematic depicting the stages of centriolar amplification and multiciliogenesis in

cultured ependymal cells. (H, I) Representative images of cultured wild-type and *Pcm1*<sup>-/-</sup> ependymal cells after 3 days of serum starvation and immunostained for basal bodies (FOP, yellow) and CEP131 (magenta, H) or PCNT (magenta, I), at the “centriolar/amplification” (C/A), “growth” (G) and “disengagement” (D) stages of centriolar amplification. White arrows indicate basal bodies. Blue arrowheads indicate elongated fibrous deposition of CEP131. Scale bars: 10  $\mu$ m (A), 5  $\mu$ m (B) 5  $\mu$ m (C), 2  $\mu$ m (H) and 1  $\mu$ m (I).

**Figure 3 - figure supplement 2. *Pcm1*<sup>-/-</sup> ependymal cells form elongated centriole-like structures.** (A) Ependymal cells from P3 wild-type and *Pcm1*<sup>-/-</sup> ventricles immunostained for FOP (yellow), actin (phalloidin, cyan) and nuclei (DAPI, blue). A single optical section basal to most basal bodies is shown. Arrows indicate elongated structures to which FOP localizes with a mean length of 5.0  $\mu$ m (standard deviation  $\pm$  1.9  $\mu$ m). (B). Percentage of wild-type and *Pcm1*<sup>-/-</sup> ependymal cells with elongated FOP-localized centriole-like structures. n = 2 wild-type and 3 *Pcm1*<sup>-/-</sup> mice. Student's t-test: \*\*\* P < 0.001. (C) *Pcm1*<sup>-/-</sup> ependymal cells from P3 ventricle immunostained for FOP (yellow), TUB<sup>Ac</sup> (magenta) and nuclei (DAPI, blue). Single channel images shown below. (D) Apical and lateral views of a *Pcm1*<sup>-/-</sup> ependymal cells from P3 ventricle immunostained for FOP (yellow), TUB<sup>Ac</sup> (magenta) and nuclei (DAPI, blue). (E) *Pcm1*<sup>-/-</sup> ependymal cell from P3 ventricle immunostained for FOP (yellow), Centrin (CETN, magenta) and nuclei (DAPI, blue). Single channel images are below. (F) TEM of *Pcm1*<sup>-/-</sup> ependymal cells from P3 ventricle. Outlined areas are shown in magnified views (right). Arrows indicate elongated fibrillar structures specific to *Pcm1*<sup>-/-</sup> cells. Scale bars: 10  $\mu$ m (A), 5  $\mu$ m (C-E), 1  $\mu$ m (F, left) and 200 nm (F, right).

**Figure 3 - figure supplement 3. Delayed expression of ciliary proteins in *Pcm1*<sup>-/-</sup> mTECs.** (A) Wild-type and *Pcm1*<sup>-/-</sup> mTECs immunostained for basal bodies (FOP, yellow), cilia (TUB<sup>Ac</sup>, magenta), and nuclei (DAPI, blue) 4, 7 or 12 days after placement at air-liquid interface (ALI). Below: single channel images from boxed areas. (B) Wild-type and *Pcm1*<sup>-/-</sup> P5 tracheas immunostained for basal bodies (FOP, yellow), cilia (TUB<sup>Ac</sup>, magenta), and actin (phalloidin, cyan). Scale bar: 10  $\mu$ m. (C) TEM of axonemes of cilia from 6 month-old wild-type and *Pcm1*<sup>-/-</sup> tracheas. Scale bar: 100 nm. (D) Percentage of axonemal abnormalities in ciliary axonemes of wild-type and *Pcm1*<sup>-/-</sup> tracheal multiciliated cells (n = 120 wild-type axonemes from 3 animals, 82 *Pcm1*<sup>-/-</sup> axonemes from 3 animals). (E) Wild-type and *Pcm1*<sup>-/-</sup> tracheal cilia beat frequencies, n = 2 per genotype, large symbol represents average for that animal, small symbols represent individual cells. (F) Wild-type and *Pcm1*<sup>-/-</sup> mTEC cilia beat frequencies. N = 3 per genotype, large symbol represents average for that animal, small symbols represent individual cells, Student's t-test: ns, not significant. (G) Heatmap of LFQ mass spectrometry analysis of wild-type and *Pcm1*<sup>-/-</sup> mTECs, depicting all

changed proteins between timepoints or genotypes at ALI D0 (unciliated), D7 (ciliating) and D21 (ciliated). Right: expansion of two clusters of proteins reduced in *Pcm1*<sup>-/-</sup> mTECs at ALI D7. Font color indicates ontology: centriolar satellite proteins are in dark blue, centrosomal proteins are in light blue, ciliary proteins are in grey, and ciliary motility proteins are in purple, and include dyneins (red) and dynein axonemal assembly factors (pink). See also **Supplementary File 5**.

**Figure 3 - video 1.** Wild-type cultured ependymal cilia beat in a coordinated way 14 days after serum withdrawal.

**Figure 3 - video 2.** *Pcm1*<sup>-/-</sup> ependymal cilia show uncoordinated, slow ciliary beat 16 days after serum withdrawal.

**Figure 3 - video 3.** *Pcm1*<sup>-/-</sup> ependymal cilia show uncoordinated, slow ciliary beat 14 days after serum withdrawal.

**Figure 3 - video 4.** Cilia of a tracheal wholemount preparation from a 3-month-old wild-type mouse beating.

**Figure 3 - video 5.** Cilia of a tracheal wholemount preparation from a 2-month-old *Pcm1*<sup>-/-</sup> mouse beating.

**Figure 3 - video 6.** Wild-type ALI12 mTEC cilia beating.

**Figure 3 - video 7.** *Pcm1*<sup>-/-</sup> ALI12 mTEC cilia beating.

**Figure 4. PCM1 is essential for centriolar satellite integrity and, in some cell types, ciliogenesis.** (A) Immunoblot of wild-type and *PCM1*<sup>-/-</sup> RPE1 cell lysates for PCM1 and GAPDH (loading control). Gel stained with Coomassie blue. (B) Wild-type and *PCM1*<sup>-/-</sup> RPE1 cells immunostained for CEP131 (yellow), centrioles (FOP, magenta), and nuclei (DAPI, blue). (C) Wild-type and *PCM1*<sup>-/-</sup> RPE1 cells immunostained for CEP290 (yellow), centrioles (γ-TUB, magenta), and nuclei (DAPI, blue). (D, E) Wild-type and *Pcm1*<sup>-/-</sup> MEFs immunostained for centrioles (γ-TUB, magenta), and nuclei (DAPI, blue) with CEP131 (D) or MIB1 (E) (yellow). (F) CEP131 intensity as a function of distance from the centrosome. *Cep131*<sup>-/-</sup> MEFs are included as a control (Hall et al., 2013). 2-way ANOVA, comparing wild-type to mutants, with Dunnett correction for multiple testing: \* P< 0.05, \*\* P< 0.01, \*\*\* P<

---

0.001. Error bars represent standard error of the mean. (G) MIB1 intensity as a function of distance from the centrosome. (H) Wild-type and *PCM1*<sup>-/-</sup> RPE1 cells immunostained for PCM1 (yellow), cilia (ARL13B, magenta), centrioles (γ-TUB, cyan) and nuclei (DAPI, blue). (I) Percentage of wild-type and *PCM1*<sup>-/-</sup> RPE1 cells serum starved for 24, 72 or 96 h that are ciliated. Bar graphs show means ± SD. Unpaired student's t-test: \*\*\* P < 0.001. n > 100 cells from 3 replicates. (J) Percentage of three control (treated with non-targeting sgRNA) and *PCM1*<sup>-/-</sup> RPE1 clonal lines, serum starved for 24 h that are ciliated. Bar graphs show means ± SEM. Unpaired Student's t-test: \*\*\* P < 0.001. n > 100 cells from 2 replicates. (K) Wild-type and *Pcm1*<sup>-/-</sup> MEFs immunostained for cilia (ARL13B, yellow), centrioles (γ-TUB, magenta) and nuclei (DAPI, blue). (L) Percentage of two *PCM1*<sup>-/-</sup> RPE1 clonal lines with and without eYFP-PCM1 expression serum starved for 24 h. Bar graphs show means ± SEM. Unpaired Student's t-test: \*\* P < 0.01, \*\*\* P < 0.001. n > 100 cells from 2 replicates. (M) Percentage of wild-type and *Pcm1*<sup>-/-</sup> MEFs serum starved for 6-36 h that are ciliated. Bar graphs show means ± SEM. n = 3 MEF lines from different embryos per genotype. Student's t-test, ns = not significant.

Scale bars: 2 μm (B), 1 μm (C), 0.5 μm (B, C insets), 5 μm (D, E), 1 μm (D, E insets), 10 μm (H, K) and 1 μm (H, K insets).

**Figure 4 - figure supplement 1. PCM1 is dispensable for ciliogenesis in MEFs.** (A) Wild-type and *Pcm1*<sup>-/-</sup> MEFs serum starved for 36 h and immunostained for ARL13B (yellow), TUB<sup>Ac</sup> (magenta) and nuclei (DAPI, blue). Scale bar: 10 μm. (B) Percentage of wild-type and *Pcm1*<sup>-/-</sup> MEFs immunostained as in (A) that were ciliated. Error bars represent SEM. n = 3 MEF lines. Student's t-test: ns, not significant. (C) Percentage of wild-type and *Pcm1*<sup>-/-</sup> MEFs serum starved and immunostained as in Figure 4I possessing the denoted centrosome number. Error bars represent SEM. n = 3 MEF lines. One way ANOVA, not significant. (D) Quantification of ciliary length in wild-type and *Pcm1*<sup>-/-</sup> MEFs serum immunostained for ARL13B. Student's t-test: ns, not significant.

**Figure 4 – video 1. Centriolar satellites frequently fuse and divide near the basal body.** Endogenous PCM1-SNAP labelled with TMR-SNAP (yellow) in *Pcm1*<sup>SNAP</sup> MEFs reveals that centriolar satellites show saltatory movement, coalescing and fragmenting around the base of cilia (SiR-tubulin, magenta). Scale bar: 3 μm.

**Figure 4 – source data 1.** Full uncropped immunoblots for Figure 4G, labelled and unlabelled.

**Figure 5. PCM1 promotes mother centriole docking to preciliary vesicles.**

(A) 3D-SIM images of Myosin-Va (MyoVa, yellow), centrioles ( $\gamma$ -TUB, cyan) and cilia (TUB<sup>Ac</sup>, magenta) in wild-type and *PCM1*<sup>-/-</sup> RPE cells 1 h after serum starvation. Scale bars: 1  $\mu$ m and 0.5  $\mu$ m for main panels and insets, respectively. (B) Percentage of wild-type and *PCM1*<sup>-/-</sup> RPE1 cells with no MyoVa at centrosomes, MyoVa at centrosomes, and MyoVa at cilia. Bar graphs show means  $\pm$  SEM. Unpaired Student's t-test compared with wild-type: \*  $P < 0.05$ , \*\*  $P < 0.005$ .  $n > 50$  cells from 2 replicates. (C) 3D-SIM images of RPE1 cells immunostained with RAB34 (yellow), centrioles ( $\gamma$ -TUB, cyan) and cilia (ARL13B, magenta). Scale bars: 1  $\mu$ m and 0.5  $\mu$ m for main panels and insets, respectively. (D) Percentage of wild-type and *PCM1*<sup>-/-</sup> RPE cells 1 h and 24 h after serum starvation exhibiting no centrosomal RAB34, RAB34 at centrosomes, and RAB34 at cilia.  $n > 100$  cells. (E) Serial-section TEM of RPE1 cells during early ciliogenesis (1 h after serum starvation). Scale bar: 200 nm. (F) Percentage of wild-type and *PCM1*<sup>-/-</sup> RPE1 cells in which TEM images demonstrate basal body association with preciliary vesicles (PCV) or ciliary vesicles (CV).  $n = 5$ -20 cells.

**Figure 5 - figure supplement 1. PCM1 is dispensable for mother centriole maturation.**

(A) Wild-type and *PCM1*<sup>-/-</sup> RPE1 cells immunostained for TALPID3 (yellow), centrioles ( $\gamma$ -TUB, cyan), and cilia (ARL13B, magenta). (B) Quantification of TALPID3 levels at centrioles. (C) Wild-type and *PCM1*<sup>-/-</sup> RPE1 cells immunostained for Centrobilin (yellow), distal appendages (CEP164, cyan) and centrioles (FOP, magenta). (D) Percentage of wild-type and *PCM1*<sup>-/-</sup> RPE1 cells with 24 h after serum starvation with the designated number of Centrobilin foci at centrioles. (E) Quantification of Centrobilin levels at centrioles 24 h after serum starvation. (F) Wild-type and *PCM1*<sup>-/-</sup> RPE1 cells immunostained for subdistal appendage protein Ninein (yellow), centrioles ( $\gamma$ -TUB, cyan), and cilia (ARL13B, magenta). (G) Quantification of Ninein levels at centrioles. (H) Wild-type and *PCM1*<sup>-/-</sup> RPE1 cells immunostained for distal appendage protein FBF1 (yellow), centrioles ( $\gamma$ -TUB, cyan), and cilia (ARL13B, magenta). (I) Quantification of FBF1 levels at mother centrioles. (J) Wild-type and *PCM1*<sup>-/-</sup> RPE1 cells immunostained for distal appendage protein ANKRD26 (yellow), centrioles ( $\gamma$ -TUB, cyan), and cilia (TUB<sup>Ac</sup>, magenta). (K) Quantification of ANKRD26 levels at mother centrioles. Scale bars: 2  $\mu$ m in main panels and 0.5  $\mu$ m in insets. Student's t-test: \*  $P < 0.05$ , \*\*\*  $P < 0.001$ , ns, not significant.

**Figure 5 - figure supplement 2. PCM1 promotes mother centriole association with vesicles.** Serial-section TEM images of wild-type (A) and *PCM1*<sup>-/-</sup> (B) RPE1 cells 1 h after serum starvation. Subdistal appendages (SDA) are denoted with yellow arrowheads and

distal appendages (DA) are denoted with red arrowheads. In *PCM1*<sup>-/-</sup> RPE1 cells, the mother centrioles were less frequently associated with a ciliary vesicle (CV). Scale bar: 500 nm.

**Figure 6. PCM1 promotes removal of CP110 and CEP97 from the mother centriole.** (A) Wild-type and *PCM1*<sup>-/-</sup> RPE1 cells serum starved for 24 h immunostained for CP110 (yellow), centrioles (FOP, cyan), and distal appendages (CEP164, magenta). (B) Wild-type and *PCM1*<sup>-/-</sup> RPE1 cells serum starved for 24 h immunostained for CEP97 (yellow), centrioles (γ-TUB, cyan), and cilia (TUB<sup>Ac</sup>, magenta). (C) Percentage of wild-type and *PCM1*<sup>-/-</sup> RPE1 cells with CP110 levels at one or two centrioles. Bar graphs show means ± SEM. Unpaired Student's t-test compared with wild-type: \*\*\* P< 0.0005. n > 50 cells from 2 replicates. (D) Percentage of wild-type and *PCM1*<sup>-/-</sup> RPE1 cells with CEP97 levels at one or two centrioles. Bar graphs show means ± SEM. Unpaired Student's t-test compared with wild-type: \*\*\* P< 0.0005. n > 50 cells from 2 replicates. (E) Wild-type and *Pcm1*<sup>-/-</sup> MEFs serum starved for 24 h and immunostained for CP110 (yellow) and cilia (TUB<sup>Ac</sup>, magenta). (F) Wild-type and *Pcm1*<sup>-/-</sup> lateral ventricular wall immunostained for CP110 (yellow), basal bodies (FOP, cyan), and nuclei (DAPI, blue). (G) Percentage of wild-type and *Pcm1*<sup>-/-</sup> MEFs serum starved for 24 h with CP110 levels at none, one or two centrioles. (H) The ratio of CP110 intensity on daughter and mother centrioles in wild-type and *Pcm1*<sup>-/-</sup> MEFs serum starved for 24 h. (I) Intensity of CP110 in wild-type and *Pcm1*<sup>-/-</sup> ependymal cells. n = 3 per genotype. Large symbols represent individual animals, small symbols represent individual cells. Student's t-test, \* P< 0.05, \*\* P< 0.01, \*\*\* P< 0.001. Scale bars represent 1 μm (main panel) and 0.5 μm (inset) (A,B), represent 5 μm (main panel) and 1 μm (inset) (E), and 2 μm (F).

**Figure 6 - figure supplement 1. PCM1 promotes removal of CP110 from basal bodies of airway multiciliated cells.** (A) Wild-type and *Pcm1*<sup>-/-</sup> wholemount trachea from P45 mice immunostained for basal bodies (FOP, magenta) and CP110 (yellow). (B) Quantification of CP110 intensity at basal bodies of wild-type and *Pcm1*<sup>-/-</sup> tracheal multiciliated cells. n = 3 per genotype. Large symbols represent individual animals, small symbols represent individual cells. Student's t-test: \*\* P< 0.01. Scale bar: 3 μm.

**Figure 7. PCM1 promotes IFT recruitment and transition zone formation.** (A) Wild-type and *PCM1*<sup>-/-</sup> RPE1 cells immunostained for IFT88 (yellow), centrioles (γ-TUB, cyan), and cilia (ARL13B, magenta). (B) Quantification of IFT88 intensity at basal bodies. (C) Immunostaining for IFT81 (yellow), centrioles (γ-TUB, cyan), and cilia (TUB<sup>Ac</sup>, magenta). (D) Quantification of IFT81 intensity at basal bodies. (E) Immunostaining for CEP162 (yellow), centrioles (γ-TUB, cyan), and cilia (ARL13B, magenta). (F) Quantification of CEP162 intensity at basal bodies. (G) Immunostaining for transition zone component RPGRIP1L

(yellow), distal appendages (CEP164, cyan), and cilia (TUB<sup>polyE</sup>, magenta). **(H)** Quantification of RPGRIP1L intensity at transition zones. **(I)** Immunostaining for TTBK2 (yellow), distal appendages (CEP164, cyan), and centrioles ( $\gamma$ -TUB, magenta). **(J)** Quantification of TTBK2 intensity at basal bodies. Scale bars in main figures represent 1  $\mu$ m and in insets represent 0.5  $\mu$ m. Student's t-test: \*  $P < 0.05$ , \*\*\*  $P < 0.001$ , ns, not significant.

**Figure 7 - figure supplement 1. PCM1 does not control IFT88 levels in MEF cilia. (A)** Wild-type and *Pcm1*<sup>-/-</sup> MEFs immunostained for IFT88 (yellow), cilia (TUB<sup>Ac</sup>, magenta) and nuclei (DAPI, blue). **(B)** Quantification of IFT88 intensity along the cilia, calculated from line plots of  $n > 120$  wild-type and *Pcm1*<sup>-/-</sup> cilia from 3 primary cell lines per genotype.

**Figure 8. PCM1 restricts CP110 and CEP97 localization to distal mother centrioles. (A)** Wild-type and *PCM1*<sup>-/-</sup> RPE1 cells immunostained for CP110 (yellow), centriolar satellites (PCM1, magenta), and nuclei (DAPI, blue) in cells with serum (cycling) or 1 h or 24 h after withdrawing serum. **(B)** Immunostaining for CEP97 (yellow), centriolar satellites (PCM1, magenta), and nuclei (DAPI, blue). **(C)** Total cell lysates of *PCM1*<sup>-/-</sup> RPE1 cell lines stably expressing eGFP or eYFP-PCM1 subjected to immunoprecipitation with anti-GFP. Precipitating proteins were immunoblotted for GFP, CP110, CEP97 and GAPDH. IP: eluate. FT: flow through. **(D)** Immunoblot of wild-type and *PCM1*<sup>-/-</sup> RPE1 cell lines lysates for CP110 and GAPDH, as well as Coomassie stain of gels. Cells were deprived of serum for 24 h prior to lysis. **(E)** Quantification of PCM1 and CP110 levels from immunoblots. **(F)** Wild-type and *PCM1*<sup>-/-</sup> RPE1 cells immunostained for CP110 (yellow) and centrioles (FOP, magenta). Cycling cells were treated with nocodazole to disperse the centriolar satellite pool of CP110, leaving the centriolar pool. **(G)** Immunostaining for CEP97 (yellow) and centrioles ( $\gamma$ -TUB, magenta) in cycling cells treated with nocodazole. **(H)** Quantification of CP110 levels at centrioles stained as in F. **(I)** Quantification of CEP97 levels at centrioles stained as in G. Scale bars: 1  $\mu$ m and 0.5  $\mu$ m in main panels and insets, respectively. Student's t-test: \*  $P < 0.05$ , \*\*\*  $P < 0.001$ , ns, not significant.

**Figure 8 - figure supplement 1. CP110 localizes to satellites in a CEP290-dependent manner. (A, B)** Cycling wild-type and *PCM1*<sup>-/-</sup> RPE1 cells immunostained for CEP290 (yellow), PCM1 (cyan) and CP110 (magenta). **(C)** Cycling wild-type RPE1 cell stained for Centrin2 (centrioles, CETN2, yellow), PCM1 (cyan) and CEP97 (magenta). **(D)** Wild-type RPE1 cells transfected with control (siGL2) or *CEP290* siRNA immunostained for CEP290 (yellow), PCM1 (cyan) and CP110 (magenta). **(E)** Immunoblot of lysates from asynchronous and synchronized wild-type and *PCM1*<sup>-/-</sup> RPE1 cells blotted for CP110 and  $\alpha$ -tubulin loading control. Scale bars: 2  $\mu$ m.

**Figure 8 – source data 1.** Full uncropped immunoblots for Figure 8C, 8I and Figure 8 - figure supplement 1E, labelled and unlabelled.

**Figure 9. Centriolar satellites remodel centrioles to promote ciliogenesis.** (A) PCM1 (cyan) scaffolds centriolar satellites, dynamic and heterogeneous condensates of centriolar proteins. During ciliogenesis, we propose that centriolar satellites remove, or wick away, CP110 and CEP97 from the mother centriole. Departure of CP110 and CEP97 is important for subsequent steps in ciliogenesis, including centriolar vesicle formation, transition zone formation and IFT-B recruitment. (B) In the absence of PCM1 and centriolar satellites, CP110 and CEP97 are not efficiently removed during ciliogenesis, disrupting subsequent steps, impeding ciliogenesis in a cell type-specific way and leading to hydrocephaly and other ciliopathy-associated phenotypes.

**Supplementary File 1. gRNAs, repair template and siRNA sequences.**

**Supplementary File 2. Genotyping primer sequences**

**Supplementary File 3. Primary antibodies**

**Supplementary File 4. Secondary antibodies**

**Supplementary File 5. Differentially expressed proteins between wild type and *Pcm1*<sup>-/-</sup> mouse tracheal epithelial cells (mTECs) on at least one timepoint (ALI1, ALI7 and/or ALI21).** Expression is given as LFQ normalized by variance stabilizing transformation as described in Materials and Methods, significantly differentially expressed proteins were defined by an FDR cutoff of 0.05.

## References

- Bankhead, P., Loughrey, M.B., Fernández, J.A., Dombrowski, Y., McArt, D.G., Dunne, P.D., McQuaid, S., Gray, R.T., Murray, L.J., Coleman, H.G., James, J.A., Salto-Tellez, M., Hamilton, P.W., 2017. QuPath: Open source software for digital pathology image analysis. *Sci. Rep.* 7, 16878. doi:10.1038/s41598-017-17204-5
- Bärenz, F., Mayilo, D., Gruss, O.J., 2011. Centriolar satellites: busy orbits around the centrosome. *Eur. J. Cell Biol.* 90, 983–989. doi:10.1016/j.ejcb.2011.07.007
- Čajánek, L., Nigg, E.A., 2014. Cep164 triggers ciliogenesis by recruiting Tau tubulin kinase 2 to the mother centriole. *Proc. Natl. Acad. Sci. USA* 111, E2841-50. doi:10.1073/pnas.1401777111
-

- 1254 Conkar, D., Bayraktar, H., Firat-Karalar, E.N., 2019. Centrosomal and ciliary targeting of  
1255 CCDC66 requires cooperative action of centriolar satellites, microtubules and  
1256 molecular motors. *Sci. Rep.* 9, 14250. doi:10.1038/s41598-019-50530-4
- 1257 Conkar, D., Culfa, E., Odabasi, E., Rauniyar, N., Yates, J.R., Firat-Karalar, E.N., 2017. The  
1258 centriolar satellite protein CCDC66 interacts with CEP290 and functions in cilium  
1259 formation and trafficking. *J. Cell Sci.* 130, 1450–1462. doi:10.1242/jcs.196832
- 1260 Cox, J., Hein, M.Y., Lubner, C.A., Paron, I., Nagaraj, N., Mann, M., 2014. Accurate  
1261 proteome-wide label-free quantification by delayed normalization and maximal  
1262 peptide ratio extraction, termed MaxLFQ. *Mol. Cell Proteomics* 13, 2513–2526.  
1263 doi:10.1074/mcp.M113.031591
- 1264 Crivat, G., Taraska, J.W., 2012. Imaging proteins inside cells with fluorescent tags. *Trends*  
1265 *Biotechnol.* 30, 8–16. doi:10.1016/j.tibtech.2011.08.002
- 1266 Dahmane, N., Ruiz i Altaba, A., 1999. Sonic hedgehog regulates the growth and patterning of  
1267 the cerebellum. *Development* 126, 3089–3100. doi:10.1242/dev.126.14.3089
- 1268 Dammermann, A., Merdes, A., 2002. Assembly of centrosomal proteins and microtubule  
1269 organization depends on PCM-1. *J. Cell Biol.* 159, 255–266.  
1270 doi:10.1083/jcb.200204023
- 1271 Delgehyr, N., Meunier, A., Faucourt, M., Bosch Grau, M., Strehl, L., Janke, C., Spassky, N.,  
1272 2015. Ependymal cell differentiation, from monociliated to multiciliated cells.  
1273 *Methods Cell Biol.* 127, 19–35. doi:10.1016/bs.mcb.2015.01.004
- 1274 Eenjes, E., Mertens, T.C.J., Buscop-van Kempen, M.J., van Wijck, Y., Taube, C., Rottier,  
1275 R.J., Hiemstra, P.S., 2018. A novel method for expansion and differentiation of mouse  
1276 tracheal epithelial cells in culture. *Sci. Rep.* 8, 7349. doi:10.1038/s41598-018-25799-  
1277 6
- 1278 Farrell, J., Kelly, C., Rauch, J., Kida, K., García-Muñoz, A., Monsefi, N., Turriziani, B.,  
1279 Doherty, C., Mehta, J.P., Matallanas, D., Simpson, J.C., Kolch, W., von Kriegsheim,  
1280 A., 2014. HGF induces epithelial-to-mesenchymal transition by modulating the  
1281 mammalian hippo/MST2 and ISG15 pathways. *J. Proteome Res.* 13, 2874–2886.  
1282 doi:10.1021/pr5000285
- 1283 Ferrante, M.I., Zullo, A., Barra, A., Bimonte, S., Messaddeq, N., Studer, M., Dollé, P.,  
1284 Franco, B., 2006. Oral-facial-digital type I protein is required for primary cilia  
1285 formation and left-right axis specification. *Nat. Genet.* 38, 112–117.  
1286 doi:10.1038/ng1684
- 1287 Findlay, A.S., Carter, R.N., Starbuck, B., McKie, L., Nováková, K., Budd, P.S., Keighren,  
1288 M.A., Marsh, J.A., Cross, S.H., Simon, M.M., Potter, P.K., Morton, N.M., Jackson,  
1289 I.J., 2018. Mouse *Idh3a* mutations cause retinal degeneration and reduced  
1290 mitochondrial function. *Dis. Model. Mech.* 11. doi:10.1242/dmm.036426
- 1291 Ganga, A.K., Kennedy, M.C., Oguchi, M.E., Gray, S., Oliver, K.E., Knight, T.A., De La  
1292 Cruz, E.M., Homma, Y., Fukuda, M., Breslow, D.K., 2021. Rab34 GTPase mediates  
1293 ciliary membrane formation in the intracellular ciliogenesis pathway. *Curr. Biol.* 31,  
1294 2895–2905.e7. doi:10.1016/j.cub.2021.04.075
- 1295 Gheiratmand, L., Coyaud, E., Gupta, G.D., Laurent, E.M., Hasegan, M., Prosser, S.L.,  
1296 Gonçalves, J., Raught, B., Pelletier, L., 2019. Spatial and proteomic profiling reveals  
1297 centrosome-independent features of centriolar satellites. *EMBO J.* 38, e101109.  
1298 doi:10.15252/embj.2018101109
- 1299 Goetz, S.C., Liem, K.F., Anderson, K.V., 2012. The spinocerebellar ataxia-associated gene  
1300 Tau tubulin kinase 2 controls the initiation of ciliogenesis. *Cell* 151, 847–858.  
1301 doi:10.1016/j.cell.2012.10.010
- 1302 Gonçalves, A.B., Hasselbalch, S.K., Joensen, B.B., Patzke, S., Martens, P., Ohlsen, S.K.,  
1303 Quinodoz, M., Nikopoulos, K., Suleiman, R., Damsø Jeppesen, M.P., Weiss, C.,

- 1304 Christensen, S.T., Rivolta, C., Andersen, J.S., Farinelli, P., Pedersen, L.B., 2021.  
 1305 CEP78 functions downstream of CEP350 to control biogenesis of primary cilia by  
 1306 negatively regulating CP110 levels. *Elife* 10. doi:10.7554/eLife.63731
- 1307 Guirao, B., Meunier, A., Mortaud, S., Aguilar, A., Corsi, J.-M., Strehl, L., Hirota, Y.,  
 1308 Desoeuvre, A., Boutin, C., Han, Y.-G., Mirzadeh, Z., Cremer, H., Montcouquiol, M.,  
 1309 Sawamoto, K., Spassky, N., 2010. Coupling between hydrodynamic forces and planar  
 1310 cell polarity orients mammalian motile cilia. *Nat. Cell Biol.* 12, 341–350.  
 1311 doi:10.1038/ncb2040
- 1312 Gupta, G.D., Coyaud, É., Gonçalves, J., Mojarad, B.A., Liu, Y., Wu, Q., Gheiratmand, L.,  
 1313 Comartin, D., Tkach, J.M., Cheung, S.W.T., Bashkurov, M., Hasegan, M., Knight,  
 1314 J.D., Lin, Z.-Y., Schueler, M., Hildebrandt, F., Moffat, J., Gingras, A.-C., Raught, B.,  
 1315 Pelletier, L., 2015. A Dynamic Protein Interaction Landscape of the Human  
 1316 Centrosome-Cilium Interface. *Cell* 163, 1484–1499. doi:10.1016/j.cell.2015.10.065
- 1317 Hall, E.A., Keighren, M., Ford, M.J., Davey, T., Jarman, A.P., Smith, L.B., Jackson, I.J.,  
 1318 Mill, P., 2013. Acute versus chronic loss of mammalian Azi1/Cep131 results in  
 1319 distinct ciliary phenotypes. *PLoS Genet.* 9, e1003928.  
 1320 doi:10.1371/journal.pgen.1003928
- 1321 Holdgaard, S.G., Cianfanelli, V., Pupo, E., Lambrugh, M., Lubas, M., Nielsen, J.C., Eibes,  
 1322 S., Maiani, E., Harder, L.M., Wesch, N., Foged, M.M., Maeda, K., Nazio, F., de la  
 1323 Ballina, L.R., Dötsch, V., Brech, A., Frankel, L.B., Jäättelä, M., Locatelli, F., Barisic,  
 1324 M., Andersen, J.S., Bekker-Jensen, S., Lund, A.H., Rogov, V.V., Papaleo, E.,  
 1325 Lanzetti, L., De Zio, D., Cecconi, F., 2019. Selective autophagy maintains centrosome  
 1326 integrity and accurate mitosis by turnover of centriolar satellites. *Nat. Commun.* 10,  
 1327 4176. doi:10.1038/s41467-019-12094-9
- 1328 Hori, A., Toda, T., 2017. Regulation of centriolar satellite integrity and its physiology. *Cell*  
 1329 *Mol. Life Sci.* 74, 213–229. doi:10.1007/s00018-016-2315-x
- 1330 Hossain, D., Javadi Esfehiani, Y., Das, A., Tsang, W.Y., 2017. Cep78 controls centrosome  
 1331 homeostasis by inhibiting EDD-DYRK2-DDB1VprBP. *EMBO Rep.* 18, 632–644.  
 1332 doi:10.15252/embr.201642377
- 1333 Huangfu, D., Liu, A., Rakeman, A.S., Murcia, N.S., Niswander, L., Anderson, K.V., 2003.  
 1334 Hedgehog signalling in the mouse requires intraflagellar transport proteins. *Nature*  
 1335 426, 83–87. doi:10.1038/nature02061
- 1336 Ishikawa, H., Marshall, W.F., 2011. Ciliogenesis: building the cell's antenna. *Nat. Rev. Mol.*  
 1337 *Cell Biol.* 12, 222–234. doi:10.1038/nrm3085
- 1338 Joachim, J., Razi, M., Judith, D., Wirth, M., Calamita, E., Encheva, V., Dynlacht, B.D.,  
 1339 Snijders, A.P., O'Reilly, N., Jefferies, H.B.J., Tooze, S.A., 2017. Centriolar Satellites  
 1340 Control GABARAP Ubiquitination and GABARAP-Mediated Autophagy. *Curr. Biol.*  
 1341 27, 2123–2136.e7. doi:10.1016/j.cub.2017.06.021
- 1342 Keppler, A., Gendreizig, S., Gronemeyer, T., Pick, H., Vogel, H., Johnsson, K., 2003. A  
 1343 general method for the covalent labeling of fusion proteins with small molecules in  
 1344 vivo. *Nat. Biotechnol.* 21, 86–89. doi:10.1038/nbt765
- 1345 Kim, J., Krishnaswami, S.R., Gleeson, J.G., 2008. CEP290 interacts with the centriolar  
 1346 satellite component PCM-1 and is required for Rab8 localization to the primary  
 1347 cilium. *Hum. Mol. Genet.* 17, 3796–3805. doi:10.1093/hmg/ddn277
- 1348 Kishimoto, N., Sawamoto, K., 2012. Planar polarity of ependymal cilia. *Differentiation.* 83,  
 1349 S86-90. doi:10.1016/j.diff.2011.10.007
- 1350 Klinger, M., Wang, W., Kuhns, S., Bärenz, F., Dräger-Meurer, S., Pereira, G., Gruss, O.J.,  
 1351 2014. The novel centriolar satellite protein SSX2IP targets Cep290 to the ciliary  
 1352 transition zone. *Mol. Biol. Cell* 25, 495–507. doi:10.1091/mbc.E13-09-0526
- 1353 Kodani, A., Yu, T.W., Johnson, J.R., Jayaraman, D., Johnson, T.L., Al-Gazali, L., Sztriha, L.,

- Partlow, J.N., Kim, H., Krup, A.L., Dammermann, A., Krogan, N.J., Walsh, C.A., Reiter, J.F., 2015. Centriolar satellites assemble centrosomal microcephaly proteins to recruit CDK2 and promote centriole duplication. *Elife* 4. doi:10.7554/eLife.07519
- Kubo, A., Sasaki, H., Yuba-Kubo, A., Tsukita, S., Shiina, N., 1999. Centriolar satellites: molecular characterization, ATP-dependent movement toward centrioles and possible involvement in ciliogenesis. *J. Cell Biol.* 147, 969–980. doi:10.1083/jcb.147.5.969
- Kubo, A., Tsukita, S., 2003. Non-membranous granular organelle consisting of PCM-1: subcellular distribution and cell-cycle-dependent assembly/disassembly. *J. Cell Sci.* 116, 919–928. doi:10.1242/jcs.00282
- Kumar, D., Rains, A., Herranz-Pérez, V., Lu, Q., Shi, X., Swaney, D.L., Stevenson, E., Krogan, N.J., Huang, B., Westlake, C., Garcia-Verdugo, J.M., Yoder, B.K., Reiter, J.F., 2021. A ciliopathy complex builds distal appendages to initiate ciliogenesis. *J. Cell Biol.* 220. doi:10.1083/jcb.202011133
- Kurtulmus, B., Wang, W., Ruppert, T., Neuner, A., Cerikan, B., Viol, L., Dueñas-Sánchez, R., Gruss, O.J., Pereira, G., 2016. WDR8 is a centriolar satellite and centriole-associated protein that promotes ciliary vesicle docking during ciliogenesis. *J. Cell Sci.* 129, 621–636. doi:10.1242/jcs.179713
- Lecland, N., Merdes, A., 2018. Centriolar satellites prevent uncontrolled degradation of centrosome proteins: a speculative review. *Cell Stress* 2, 20–24. doi:10.15698/cst2018.02.122
- Lee, J.Y., Stearns, T., 2013. FOP is a centriolar satellite protein involved in ciliogenesis. *PLoS One* 8, e58589. doi:10.1371/journal.pone.0058589
- Lopes, C.A.M., Prosser, S.L., Romio, L., Hirst, R.A., O’Callaghan, C., Woolf, A.S., Fry, A.M., 2011. Centriolar satellites are assembly points for proteins implicated in human ciliopathies, including oral-facial-digital syndrome 1. *J. Cell Sci.* 124, 600–612. doi:10.1242/jcs.077156
- Loukil, A., Tormanen, K., Sütterlin, C., 2017. The daughter centriole controls ciliogenesis by regulating Neurl-4 localization at the centrosome. *J. Cell Biol.* 216, 1287–1300. doi:10.1083/jcb.201608119
- Lu, Q., Insinna, C., Ott, C., Stauffer, J., Pintado, P.A., Rahajeng, J., Baxa, U., Walia, V., Cuenca, A., Hwang, Y.-S., Daar, I.O., Lopes, S., Lippincott-Schwartz, J., Jackson, P.K., Caplan, S., Westlake, C.J., 2015. Early steps in primary cilium assembly require EHD1/EHD3-dependent ciliary vesicle formation. *Nat. Cell Biol.* 17, 228–240. doi:10.1038/ncb3109
- Mazo, G., Soplop, N., Wang, W.-J., Uryu, K., Tsou, M.F.B., 2016. Spatial Control of Primary Ciliogenesis by Subdistal Appendages Alters Sensation-Associated Properties of Cilia. *Dev. Cell* 39, 424–437. doi:10.1016/j.devcel.2016.10.006
- Mercey, O., Al Jord, A., Rostaing, P., Mahuzier, A., Fortoul, A., Boudjema, A.-R., Faucourt, M., Spassky, N., Meunier, A., 2019a. Dynamics of centriole amplification in centrosome-depleted brain multiciliated progenitors. *Sci. Rep.* 9, 13060. doi:10.1038/s41598-019-49416-2
- Mercey, O., Levine, M.S., LoMastro, G.M., Rostaing, P., Brotslaw, E., Gomez, V., Kumar, A., Spassky, N., Mitchell, B.J., Meunier, A., Holland, A.J., 2019b. Massive centriole production can occur in the absence of deuterosomes in multiciliated cells. *Nat. Cell Biol.* 21, 1544–1552. doi:10.1038/s41556-019-0427-x
- Mikule, K., Delaval, B., Kaldis, P., Jurczyk, A., Hergert, P., Doxsey, S., 2007. Loss of centrosome integrity induces p38-p53-p21-dependent G1-S arrest. *Nat. Cell Biol.* 9, 160–170. doi:10.1038/ncb1529
- Mirzadeh, Z., Doetsch, F., Sawamoto, K., Wichterle, H., Alvarez-Buylla, A., 2010a. The subventricular zone en-face: wholemount staining and ependymal flow. *J. Vis. Exp.*

- doi:10.3791/1938
- Mirzadeh, Z., Han, Y.-G., Soriano-Navarro, M., García-Verdugo, J.M., Alvarez-Buylla, A., 2010b. Cilia organize ependymal planar polarity. *J. Neurosci.* 30, 2600–2610. doi:10.1523/JNEUROSCI.3744-09.2010
- Monroe, T.O., Garrett, M.E., Kousi, M., Rodriguiz, R.M., Moon, S., Bai, Y., Brodar, S.C., Soldano, K.L., Savage, J., Hansen, T.F., Muzny, D.M., Gibbs, R.A., Barak, L., Sullivan, P.F., Ashley-Koch, A.E., Sawa, A., Wetsel, W.C., Werge, T., Katsanis, N., 2020. PCM1 is necessary for focal ciliary integrity and is a candidate for severe schizophrenia. *Nat. Commun.* 11, 5903. doi:10.1038/s41467-020-19637-5
- Nanjundappa, R., Kong, D., Shim, K., Stearns, T., Brody, S.L., Loncarek, J., Mahjoub, M.R., 2019. Regulation of cilia abundance in multiciliated cells. *Elife* 8. doi:10.7554/eLife.44039
- Nigg, E.A., Holland, A.J., 2018. Once and only once: mechanisms of centriole duplication and their deregulation in disease. *Nat. Rev. Mol. Cell Biol.* 19, 297–312. doi:10.1038/nrm.2017.127
- Odabasi, E., Batman, U., Firat-Karalar, E.N., 2020. Unraveling the mysteries of centriolar satellites: time to rewrite the textbooks about the centrosome/cilium complex. *Mol. Biol. Cell* 31, 866–872. doi:10.1091/mbc.E19-07-0402
- Odabasi, E., Gul, S., Kavakli, I.H., Firat-Karalar, E.N., 2019. Centriolar satellites are required for efficient ciliogenesis and ciliary content regulation. *EMBO Rep.* 20. doi:10.15252/embr.201947723
- Prosser, S.L., Pelletier, L., 2020. Centriolar satellite biogenesis and function in vertebrate cells. *J. Cell Sci.* 133. doi:10.1242/jcs.239566
- Prosser, S.L., Tkach, J., Gheiratmand, L., Kim, J., Raught, B., Morrison, C.G., Pelletier, L., 2022. Aggresome assembly at the centrosome is driven by CP110-CEP97-CEP290 and centriolar satellites. *Nat. Cell Biol.* 24, 483–496. doi:10.1038/s41556-022-00869-0
- Quarantotti, V., Chen, J.-X., Tischer, J., Gonzalez Tejedo, C., Papachristou, E.K., D'Santos, C.S., Kilmartin, J.V., Miller, M.L., Gergely, F., 2019. Centriolar satellites are acentriolar assemblies of centrosomal proteins. *EMBO J.* 38, e101082. doi:10.15252/embj.2018101082
- Quidwai, T., Wang, J., Hall, E.A., Petriman, N.A., Leng, W., Kiesel, P., Wells, J.N., Murphy, L.C., Keighren, M.A., Marsh, J.A., Lorentzen, E., Pigino, G., Mill, P., 2021. A WDR35-dependent coat protein complex transports ciliary membrane cargo vesicles to cilia. *Elife* 10. doi:10.7554/eLife.69786
- Reiter, J.F., Leroux, M.R., 2017. Genes and molecular pathways underpinning ciliopathies. *Nat. Rev. Mol. Cell Biol.* 18, 533–547. doi:10.1038/nrm.2017.60
- Ritchie, M.E., Phipson, B., Wu, D., Hu, Y., Law, C.W., Shi, W., Smyth, G.K., 2015. limma powers differential expression analyses for RNA-sequencing and microarray studies. *Nucleic Acids Res.* 43, e47. doi:10.1093/nar/gkv007
- Schindelin, J., Arganda-Carreras, I., Frise, E., Kaynig, V., Longair, M., Pietzsch, T., Preibisch, S., Rueden, C., Saalfeld, S., Schmid, B., Tinevez, J.-Y., White, D.J., Hartenstein, V., Eliceiri, K., Tomancak, P., Cardona, A., 2012. Fiji: an open-source platform for biological-image analysis. *Nat. Methods* 9, 676–682. doi:10.1038/nmeth.2019
- Schmidt, K.N., Kuhns, S., Neuner, A., Hub, B., Zentgraf, H., Pereira, G., 2012. Cep164 mediates vesicular docking to the mother centriole during early steps of ciliogenesis. *J. Cell Biol.* 199, 1083–1101. doi:10.1083/jcb.201202126
- Schmidt, T.I., Kleylein-Sohn, J., Westendorf, J., Le Clech, M., Lavoie, S.B., Stierhof, Y.-D., Nigg, E.A., 2009. Control of centriole length by CPAP and CP110. *Curr. Biol.* 19,

- 1454 1005–1011. doi:10.1016/j.cub.2009.05.016
- 1455 Shen, X.-L., Yuan, J.-F., Qin, X.-H., Song, G.-P., Hu, H.-B., Tu, H.-Q., Song, Z.-Q., Li, P.-
- 1456 Y., Xu, Y.-L., Li, S., Jian, X.-X., Li, J.-N., He, C.-Y., Yu, X.-P., Liang, L.-Y., Wu,
- 1457 M., Han, Q.-Y., Wang, K., Li, A.-L., Zhou, T., Zhang, Y.-C., Wang, N., Li, H.-Y.,
- 1458 2022. LUBAC regulates ciliogenesis by promoting CP110 removal from the mother
- 1459 centriole. *J. Cell Biol.* 221. doi:10.1083/jcb.202105092
- 1460 Sillibourne, J.E., Hurbain, I., Grand-Perret, T., Goud, B., Tran, P., Bornens, M., 2013.
- 1461 Primary ciliogenesis requires the distal appendage component Cep123. *Biol. Open* 2,
- 1462 535–545. doi:10.1242/bio.20134457
- 1463 Spassky, N., Han, Y.G., Aguilar, A., Strehl, L., Besse, L., Laclef, C., Ros, M.R., Garcia-
- 1464 Verdugo, J.M., Alvarez-Buylla, A., 2008. Primary cilia are required for cerebellar
- 1465 development and Shh-dependent expansion of progenitor pool. *Dev. Biol.* 317, 246–
- 1466 259. doi:10.1016/j.ydbio.2008.02.026
- 1467 Spektor, A., Tsang, W.Y., Khoo, D., Dynlacht, B.D., 2007. Cep97 and CP110 suppress a cilia
- 1468 assembly program. *Cell* 130, 678–690. doi:10.1016/j.cell.2007.06.027
- 1469 Staples, C.J., Myers, K.N., Beveridge, R.D.D., Patil, A.A., Howard, A.E., Barone, G., Lee,
- 1470 A.J.X., Swanton, C., Howell, M., Maslen, S., Skehel, J.M., Boulton, S.J., Collis, S.J.,
- 1471 2014. Ccdc13 is a novel human centriolar satellite protein required for ciliogenesis
- 1472 and genome stability. *J. Cell Sci.* 127, 2910–2919. doi:10.1242/jcs.147785
- 1473 Staples, C.J., Myers, K.N., Beveridge, R.D.D., Patil, A.A., Lee, A.J.X., Swanton, C., Howell,
- 1474 M., Boulton, S.J., Collis, S.J., 2012. The centriolar satellite protein Cep131 is
- 1475 important for genome stability. *J. Cell Sci.* 125, 4770–4779. doi:10.1242/jcs.104059
- 1476 Stephen, L.A., Tawamie, H., Davis, G.M., Tebbe, L., Nürnberg, P., Nürnberg, G., Thiele, H.,
- 1477 Thoenes, M., Boltshauser, E., Uebe, S., Rompel, O., Reis, A., Ekici, A.B., McTeir, L.,
- 1478 Fraser, A.M., Hall, E.A., Mill, P., Daudet, N., Cross, C., Wolfrum, U., Jamra, R.A.,
- 1479 Davey, M.G., Bolz, H.J., 2015. TALPID3 controls centrosome and cell polarity and
- 1480 the human ortholog KIAA0586 is mutated in Joubert syndrome (JBTS23). *Elife* 4.
- 1481 doi:10.7554/eLife.08077
- 1482 Stirling, D.R., Swain-Bowden, M.J., Lucas, A.M., Carpenter, A.E., Cimini, B.A., Goodman,
- 1483 A., 2021. CellProfiler 4: improvements in speed, utility and usability. *BMC*
- 1484 *Bioinformatics* 22, 433. doi:10.1186/s12859-021-04344-9
- 1485 Tang, Z., Lin, M.G., Stowe, T.R., Chen, S., Zhu, M., Stearns, T., Franco, B., Zhong, Q.,
- 1486 2013. Autophagy promotes primary ciliogenesis by removing OFD1 from centriolar
- 1487 satellites. *Nature* 502, 254–257. doi:10.1038/nature12606
- 1488 Tanos, B.E., Yang, H.-J., Soni, R., Wang, W.-J., Macaluso, F.P., Asara, J.M., Tsou, M.-F.B.,
- 1489 2013. Centriole distal appendages promote membrane docking, leading to cilia
- 1490 initiation. *Genes Dev.* 27, 163–168. doi:10.1101/gad.207043.112
- 1491 Tollenaere, M.A.X., Villumsen, B.H., Blasius, M., Nielsen, J.C., Wagner, S.A., Bartek, J.,
- 1492 Beli, P., Maitland, N., Bekker-Jensen, S., 2015. p38- and MK2-dependent signalling
- 1493 promotes stress-induced centriolar satellite remodelling via 14-3-3-dependent
- 1494 sequestration of CEP131/AZI1. *Nat. Commun.* 6, 10075. doi:10.1038/ncomms10075
- 1495 Tsang, W.Y., Bossard, C., Khanna, H., Peränen, J., Swaroop, A., Malhotra, V., Dynlacht,
- 1496 B.D., 2008. CP110 suppresses primary cilia formation through its interaction with
- 1497 CEP290, a protein deficient in human ciliary disease. *Dev. Cell* 15, 187–197.
- 1498 doi:10.1016/j.devcel.2008.07.004
- 1499 Tyanova, S., Temu, T., Sinitcyn, P., Carlson, A., Hein, M.Y., Geiger, T., Mann, M., Cox, J.,
- 1500 2016. The Perseus computational platform for comprehensive analysis of
- 1501 (prote)omics data. *Nat. Methods* 13, 731–740. doi:10.1038/nmeth.3901
- 1502 Villumsen, B.H., Danielsen, J.R., Povlsen, L., Sylvestersen, K.B., Merdes, A., Beli, P., Yang,
- 1503 Y.-G., Choudhary, C., Nielsen, M.L., Maitland, N., Bekker-Jensen, S., 2013. A new

- cellular stress response that triggers centriolar satellite reorganization and ciliogenesis. *EMBO J.* 32, 3029–3040. doi:10.1038/emboj.2013.223
- Vladar, E.K., Stearns, T., 2007. Molecular characterization of centriole assembly in ciliated epithelial cells. *J. Cell Biol.* 178, 31–42. doi:10.1083/jcb.200703064
- Walentek, P., Quigley, I.K., Sun, D.I., Sajjan, U.K., Kintner, C., Harland, R.M., 2016. Ciliary transcription factors and miRNAs precisely regulate Cp110 levels required for ciliary adhesions and ciliogenesis. *Elife* 5. doi:10.7554/eLife.17557
- Wallace, V.A., 1999. Purkinje-cell-derived Sonic hedgehog regulates granule neuron precursor cell proliferation in the developing mouse cerebellum. *Curr. Biol.* 9, 445–448. doi:10.1016/s0960-9822(99)80195-x
- Wang, G., Chen, Q., Zhang, X., Zhang, B., Zhuo, X., Liu, J., Jiang, Q., Zhang, C., 2013. PCM1 recruits Plk1 to the pericentriolar matrix to promote primary cilia disassembly before mitotic entry. *J. Cell Sci.* 126, 1355–1365. doi:10.1242/jcs.114918
- Wang, L., Failler, M., Fu, W., Dynlacht, B.D., 2018. A distal centriolar protein network controls organelle maturation and asymmetry. *Nat. Commun.* 9, 3938. doi:10.1038/s41467-018-06286-y
- Wang, L., Lee, K., Malonis, R., Sanchez, I., Dynlacht, B.D., 2016. Tethering of an E3 ligase by PCM1 regulates the abundance of centrosomal KIAA0586/Talpid3 and promotes ciliogenesis. *Elife* 5. doi:10.7554/eLife.12950
- Wang, W.-J., Tay, H.G., Soni, R., Perumal, G.S., Goll, M.G., Macaluso, F.P., Asara, J.M., Amack, J.D., Tsou, M.-F.B., 2013. CEP162 is an axoneme-recognition protein promoting ciliary transition zone assembly at the cilia base. *Nat. Cell Biol.* 15, 591–601. doi:10.1038/ncb2739
- Wechsler-Reya, R.J., Scott, M.P., 1999. Control of neuronal precursor proliferation in the cerebellum by Sonic Hedgehog. *Neuron* 22, 103–114. doi:10.1016/s0896-6273(00)80682-0
- Wiśniewski, J.R., Mann, M., 2012. Consecutive proteolytic digestion in an enzyme reactor increases depth of proteomic and phosphoproteomic analysis. *Anal. Chem.* 84, 2631–2637. doi:10.1021/ac300006b
- Wu, C.-T., Chen, H.-Y., Tang, T.K., 2018. Myosin-Va is required for preciliary vesicle transportation to the mother centriole during ciliogenesis. *Nat. Cell Biol.* 20, 175–185. doi:10.1038/s41556-017-0018-7
- Yadav, S.P., Sharma, N.K., Liu, C., Dong, L., Li, T., Swaroop, A., 2016. Centrosomal protein CP110 controls maturation of the mother centriole during cilia biogenesis. *Development* 143, 1491–1501. doi:10.1242/dev.130120
- You, Y., Richer, E.J., Huang, T., Brody, S.L., 2002. Growth and differentiation of mouse tracheal epithelial cells: selection of a proliferative population. *Am. J. Physiol. Lung Cell Mol. Physiol.* 283, L1315–21. doi:10.1152/ajplung.00169.2002
- Yu, J., Carroll, T.J., McMahon, A.P., 2002. Sonic hedgehog regulates proliferation and differentiation of mesenchymal cells in the mouse metanephric kidney. *Development* 129, 5301–5312. doi:10.1242/dev.129.22.5301
- Zhang, X., Smits, A.H., van Tilburg, G.B., Ovaa, H., Huber, W., Vermeulen, M., 2018. Proteome-wide identification of ubiquitin interactions using UbIA-MS. *Nat. Protoc.* 13, 530–550. doi:10.1038/nprot.2017.147
- Zhao, H., Chen, Q., Fang, C., Huang, Q., Zhou, J., Yan, X., Zhu, X., 2019. Parental centrioles are dispensable for deuterosome formation and function during basal body amplification. *EMBO Rep.* 20. doi:10.15252/embr.201846735
- Zhao, H., Chen, Q., Li, F., Cui, L., Xie, L., Huang, Q., Liang, X., Zhou, J., Yan, X., Zhu, X., 2021. Fibrogranular materials function as organizers to ensure the fidelity of multiciliary assembly. *Nat. Commun.* 12, 1273. doi:10.1038/s41467-021-21506-8

1554 Zhao, H., Zhu, L., Zhu, Y., Cao, J., Li, S., Huang, Q., Xu, T., Huang, X., Yan, X., Zhu, X.,  
1555 2013. The Cep63 paralogue Deup1 enables massive de novo centriole biogenesis for  
1556 vertebrate multiciliogenesis. *Nat. Cell Biol.* 15, 1434–1444. doi:10.1038/ncb2880  
1557

---

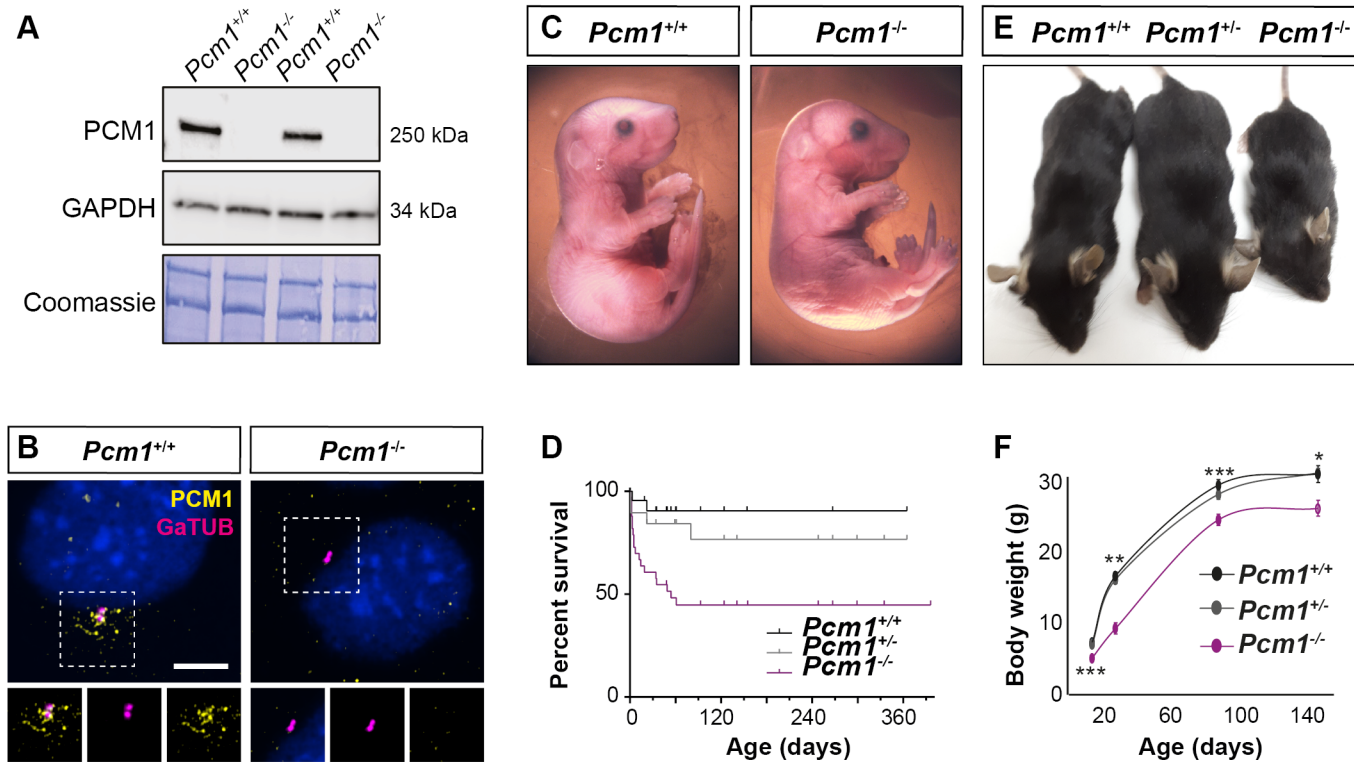


Figure 1

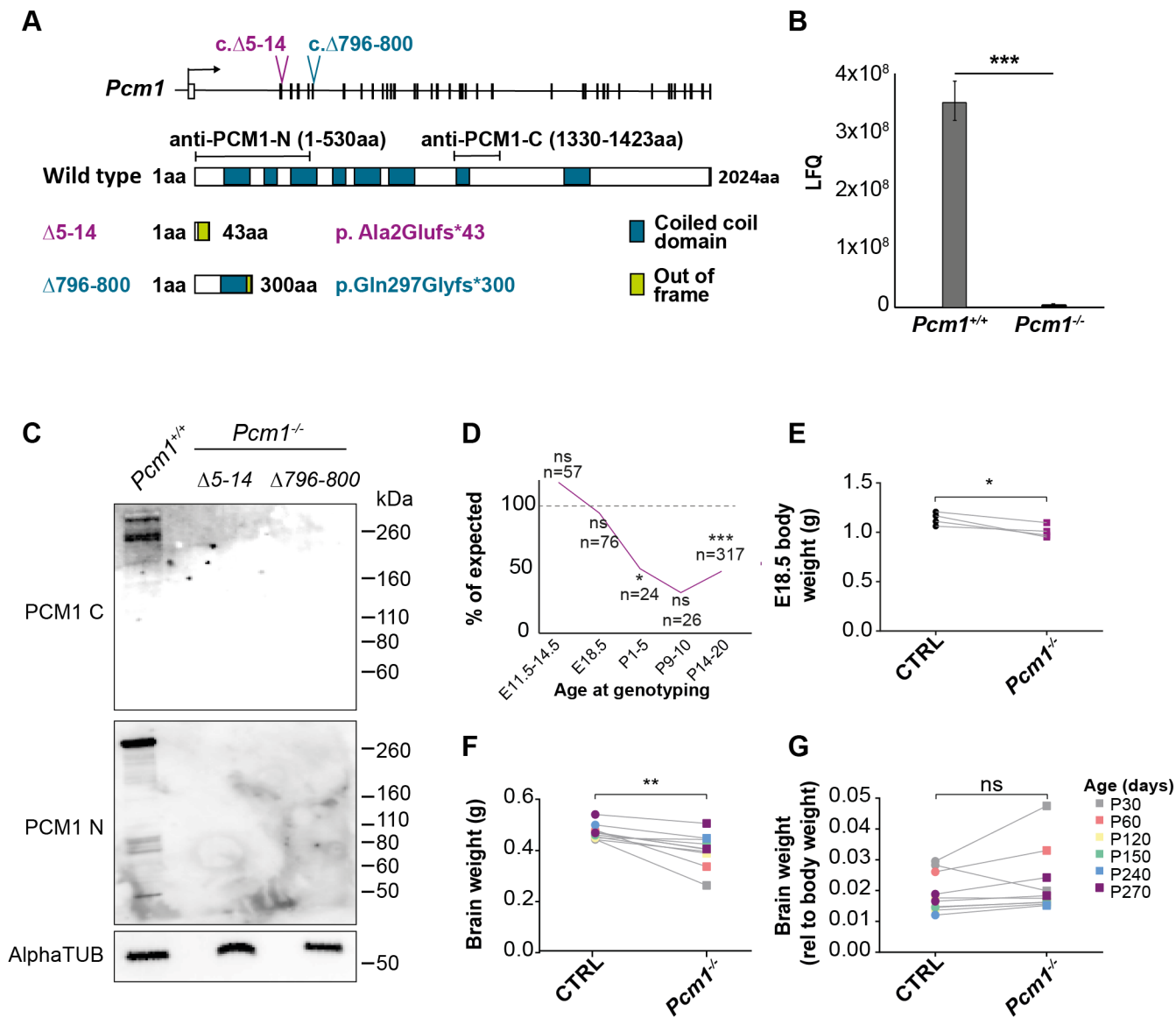


Figure 1 - figure supplement 1

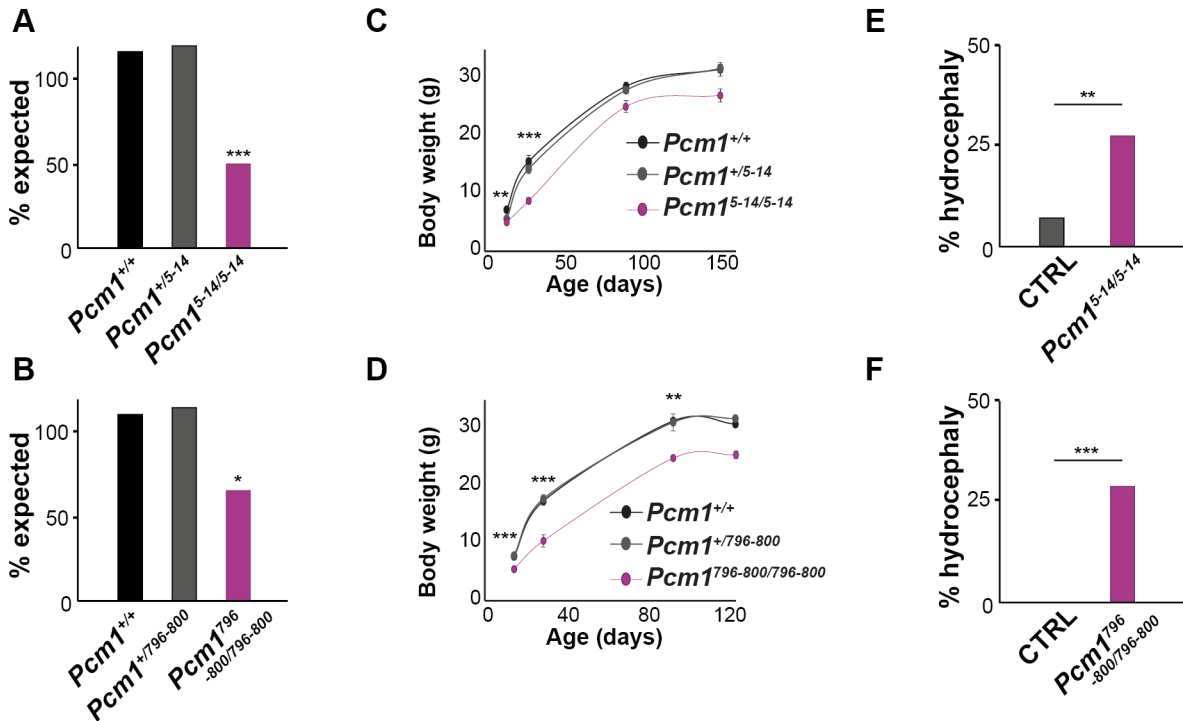


Figure 1 - figure supplement 2

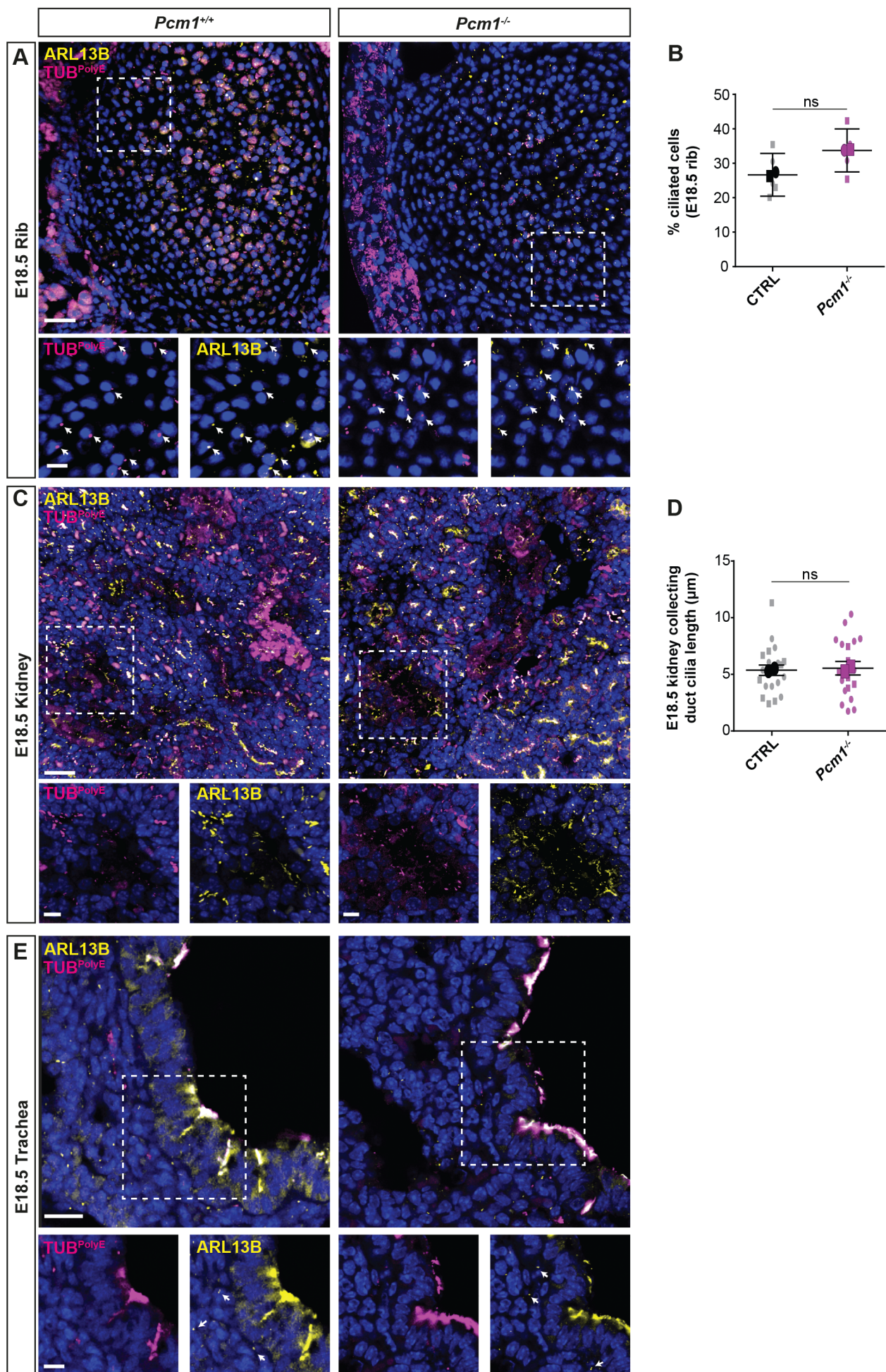


Figure 1 - figure supplement 3

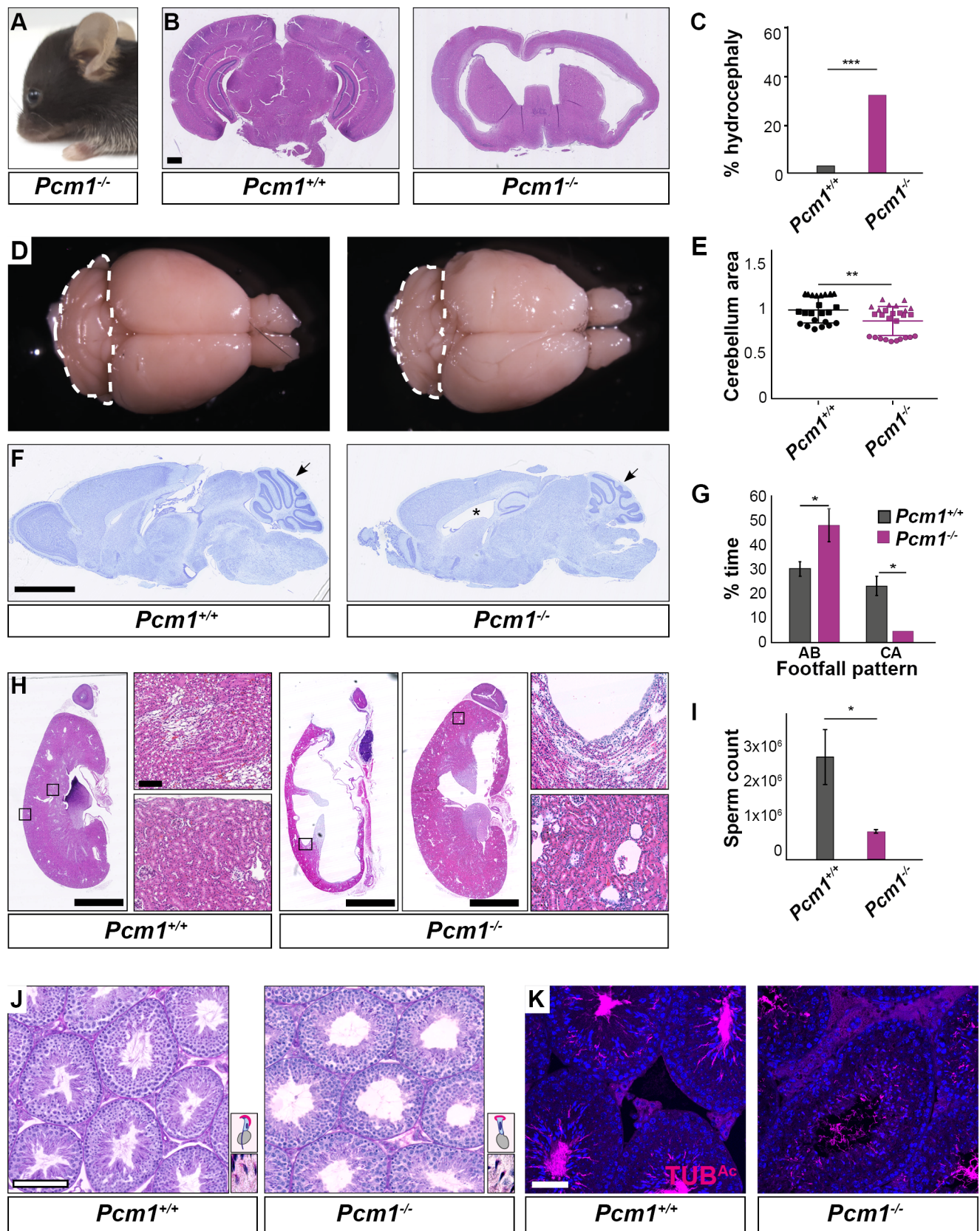


Figure 2

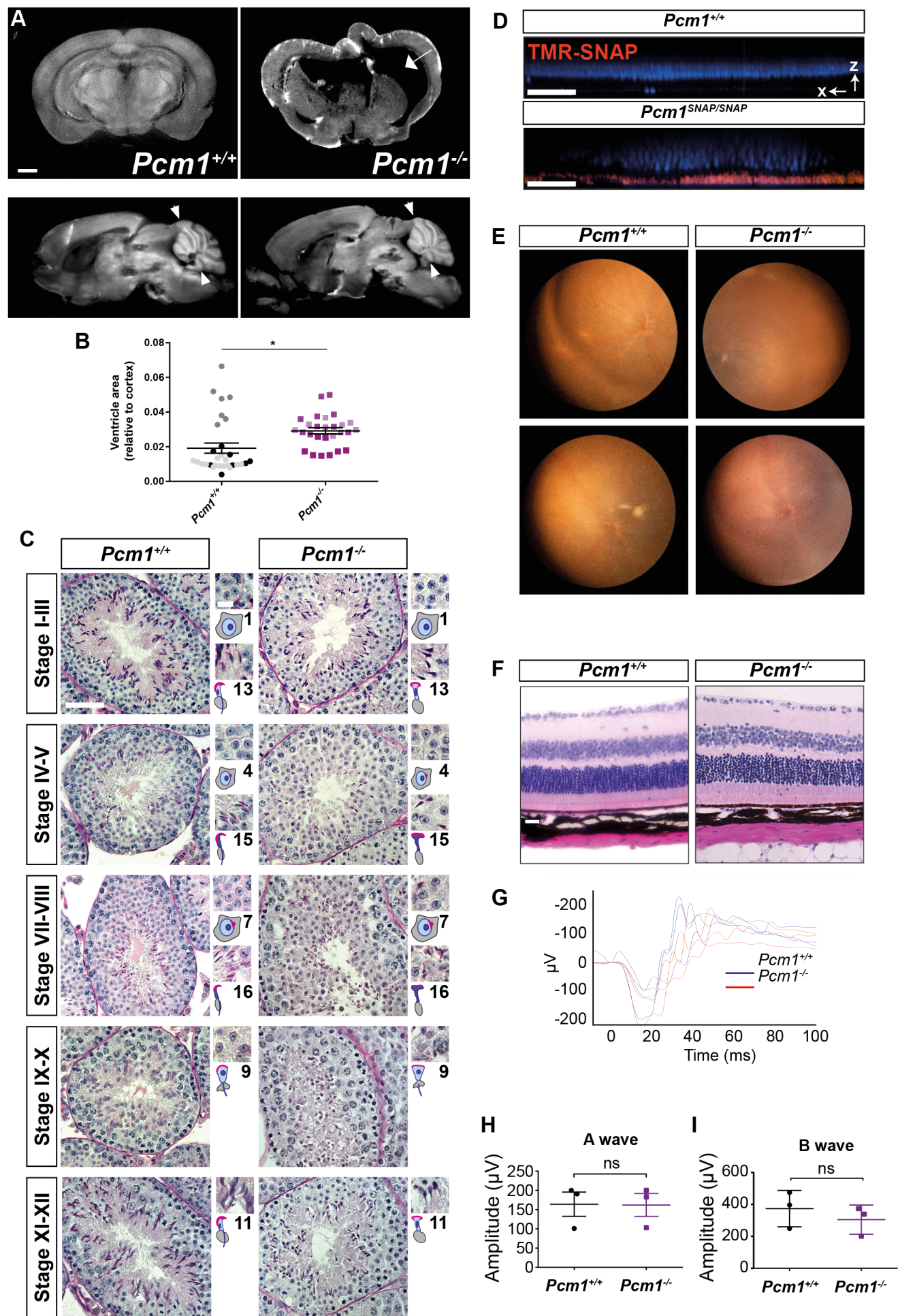


Figure 2 - figure supplement 1



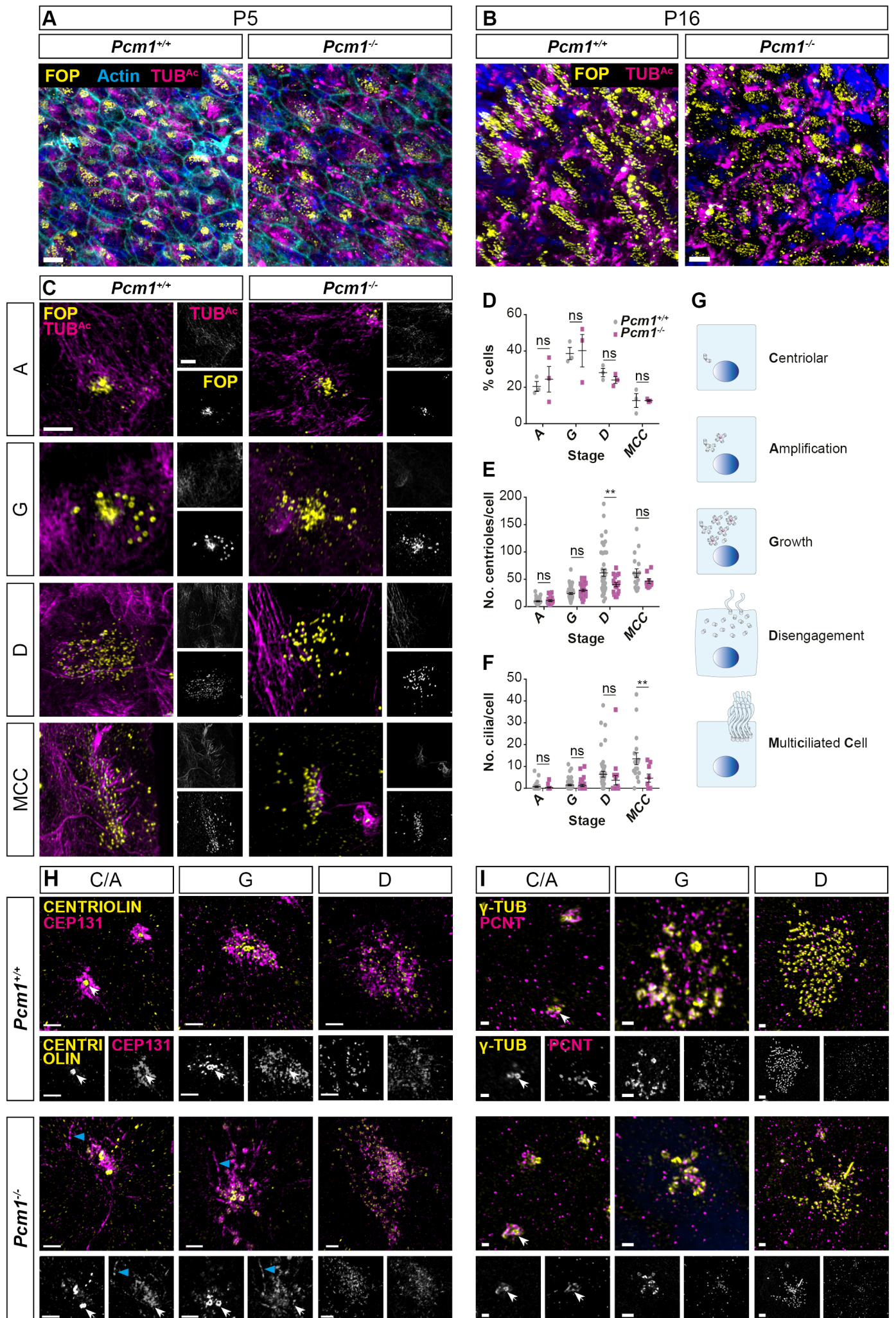
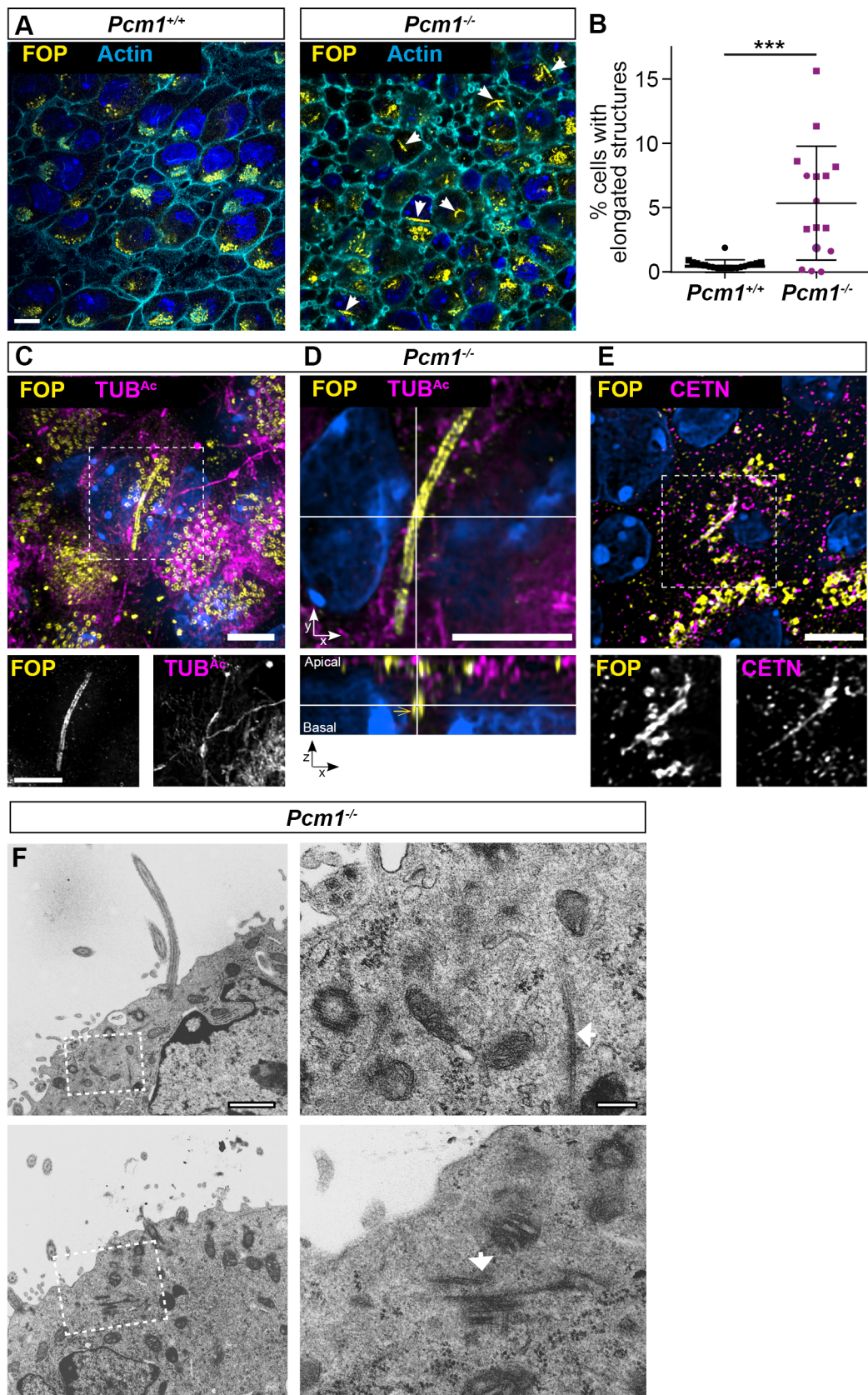


Figure 3 - figure supplement 1



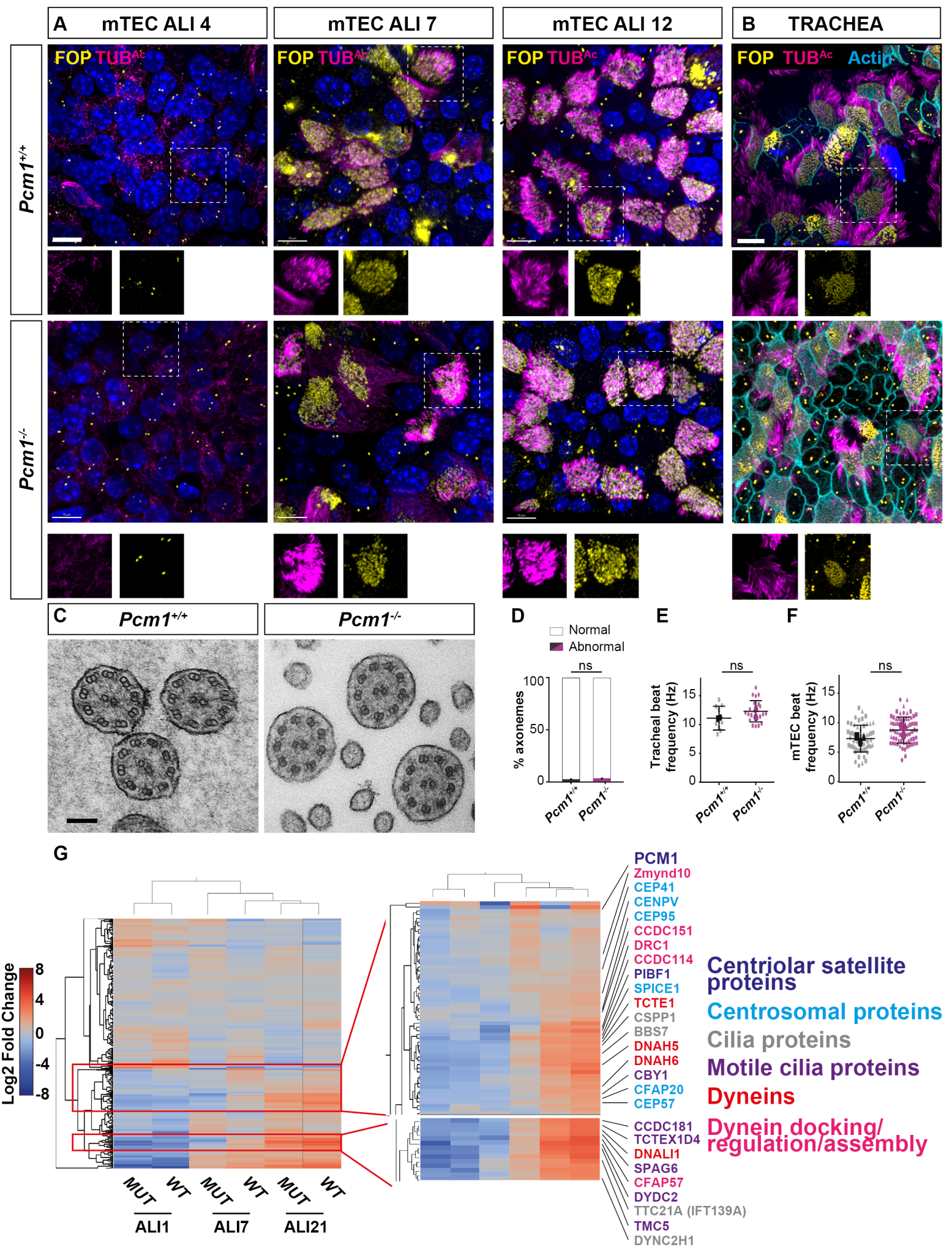


Figure 3 - figure supplement 3

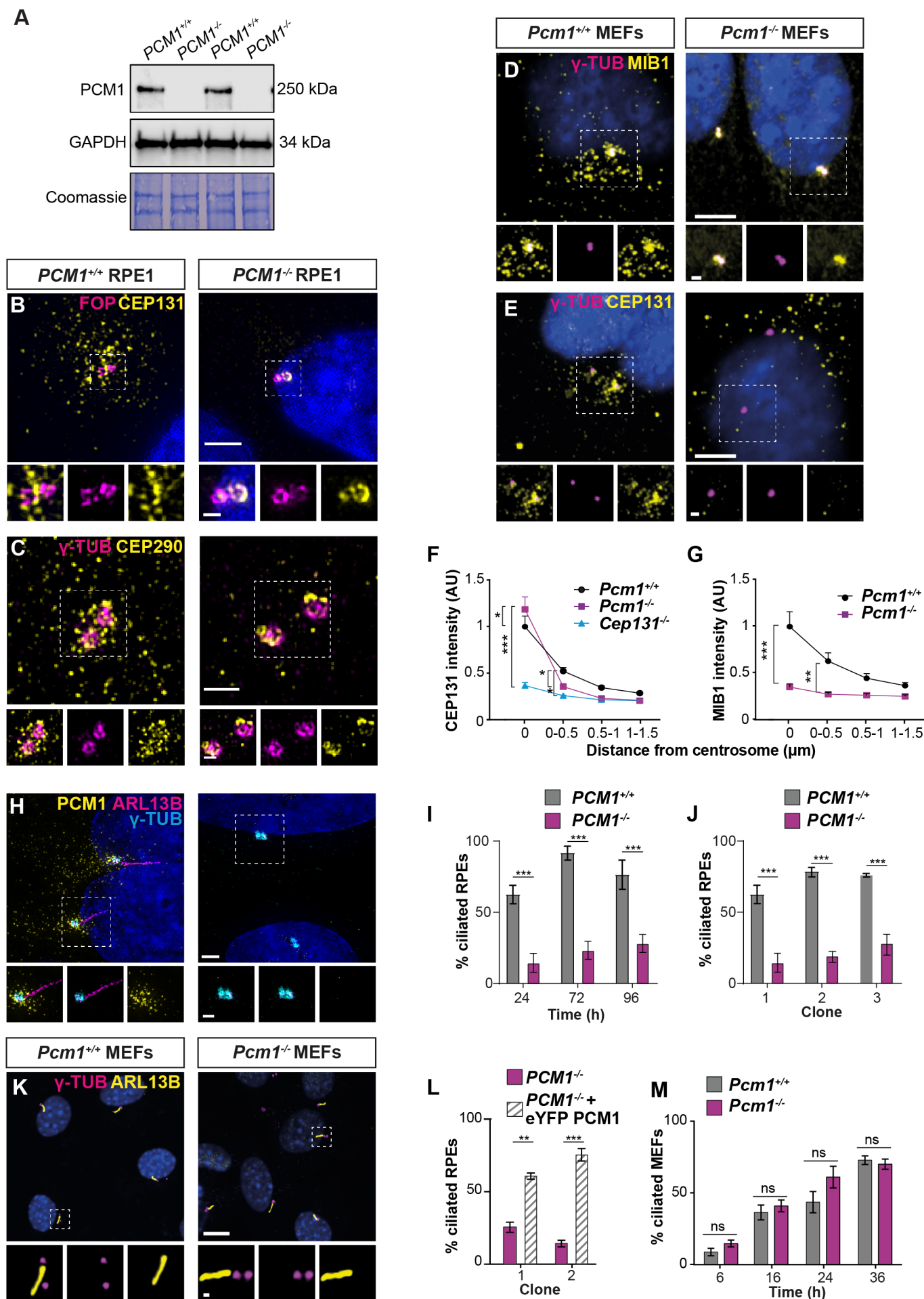


Figure 4

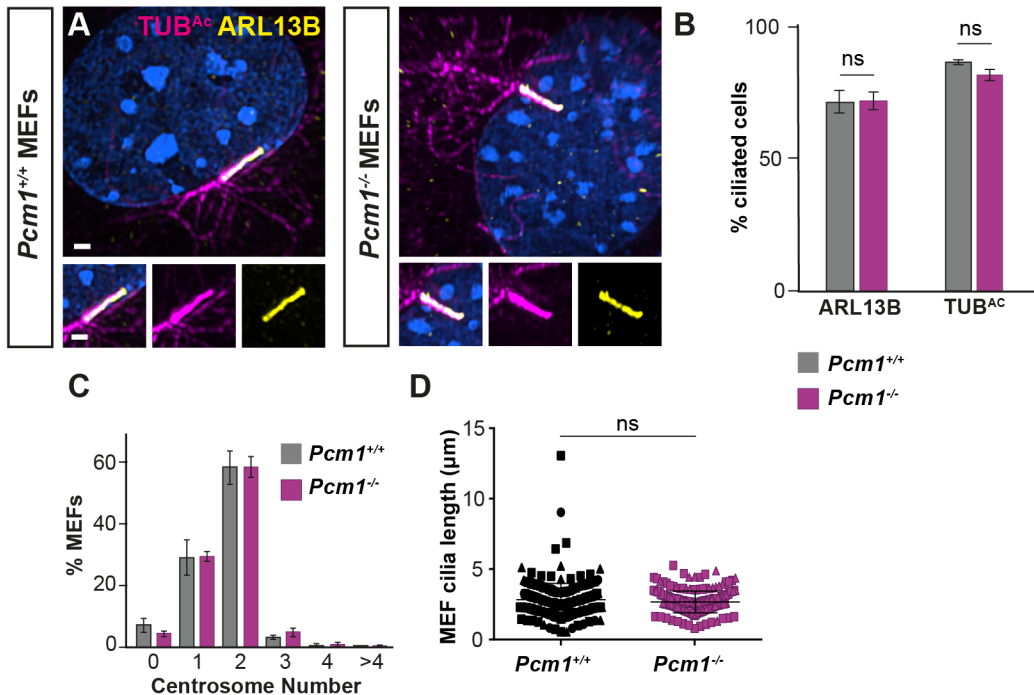


Figure 4 - figure supplement 1

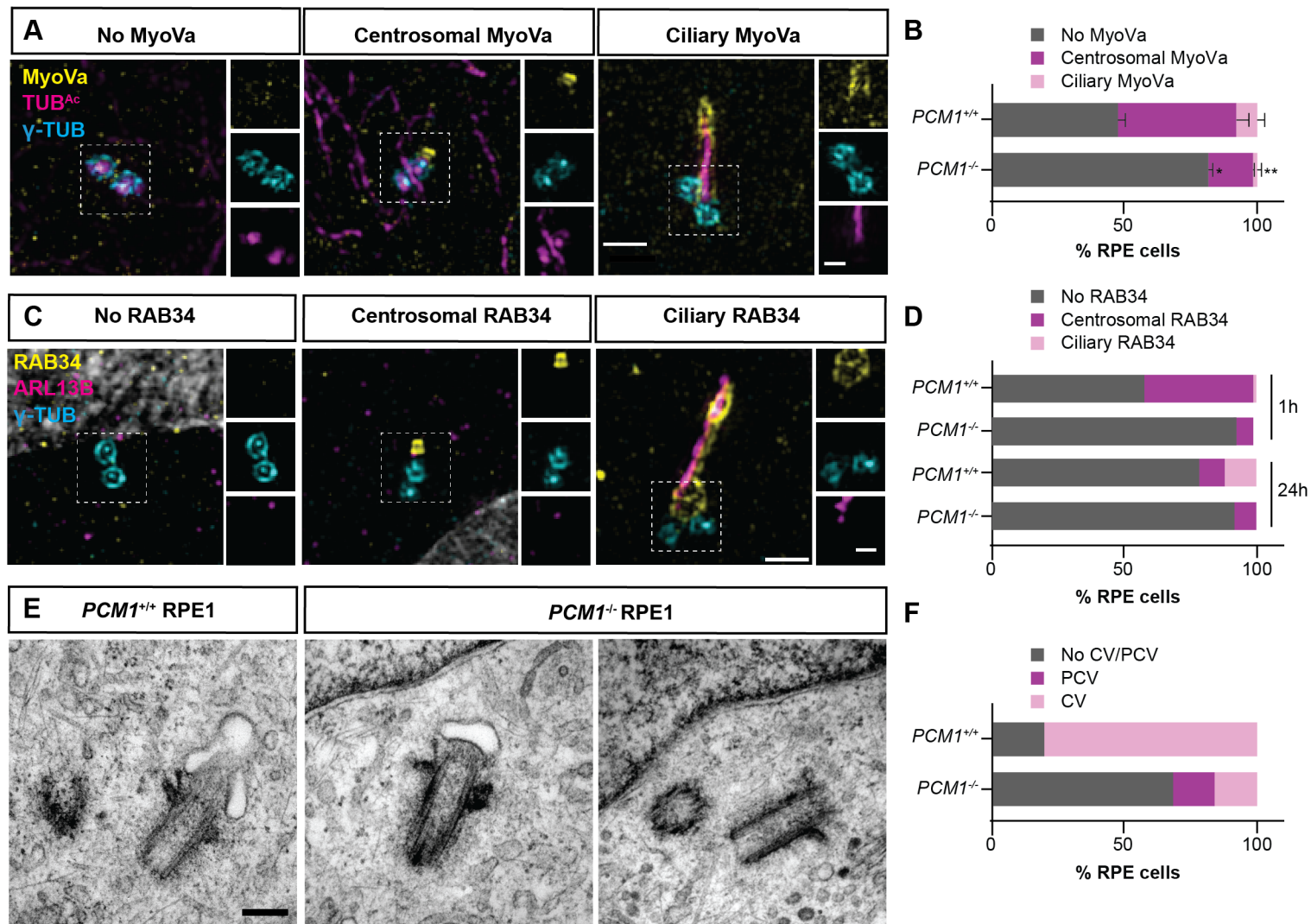


Figure 5

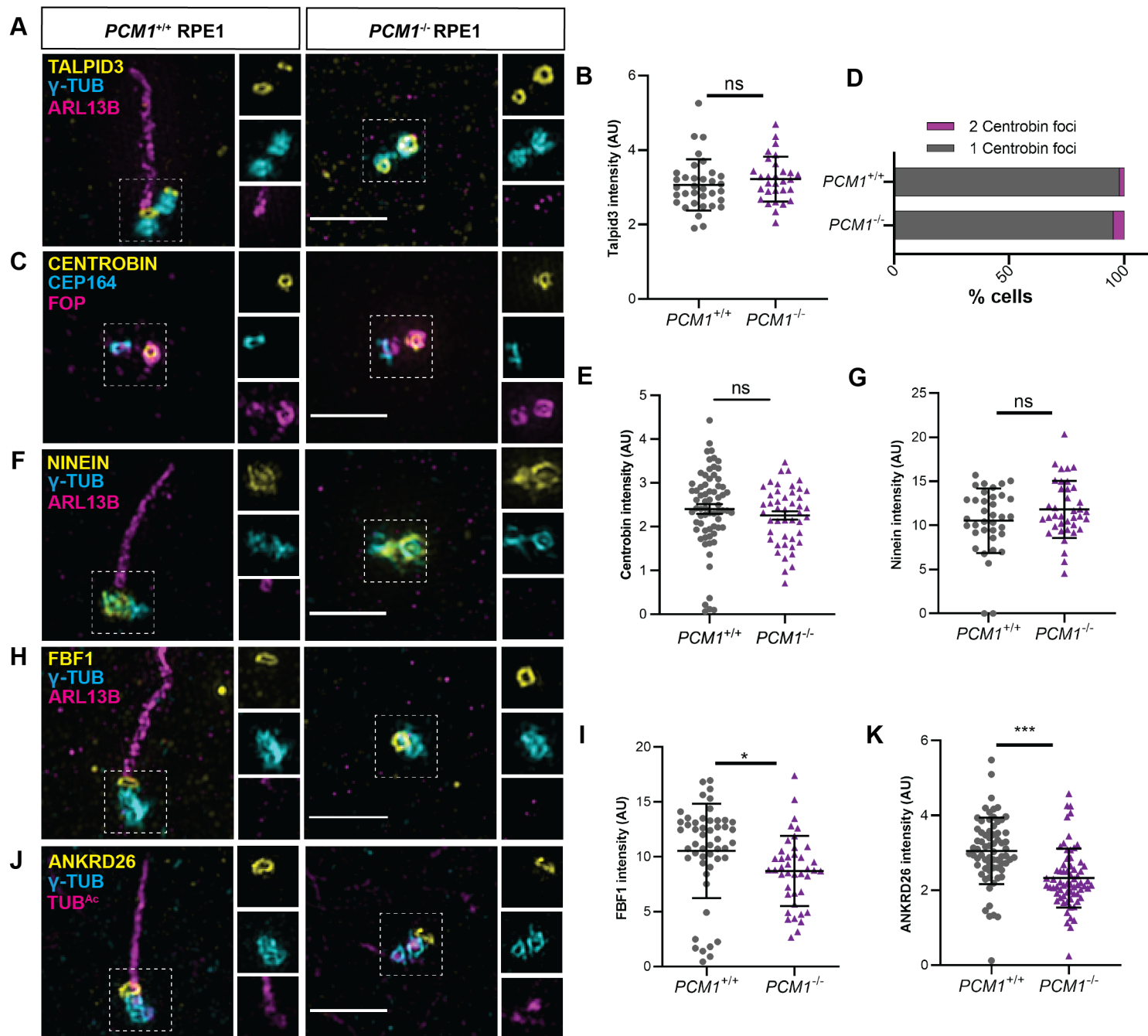


Figure 5 - figure supplement 1

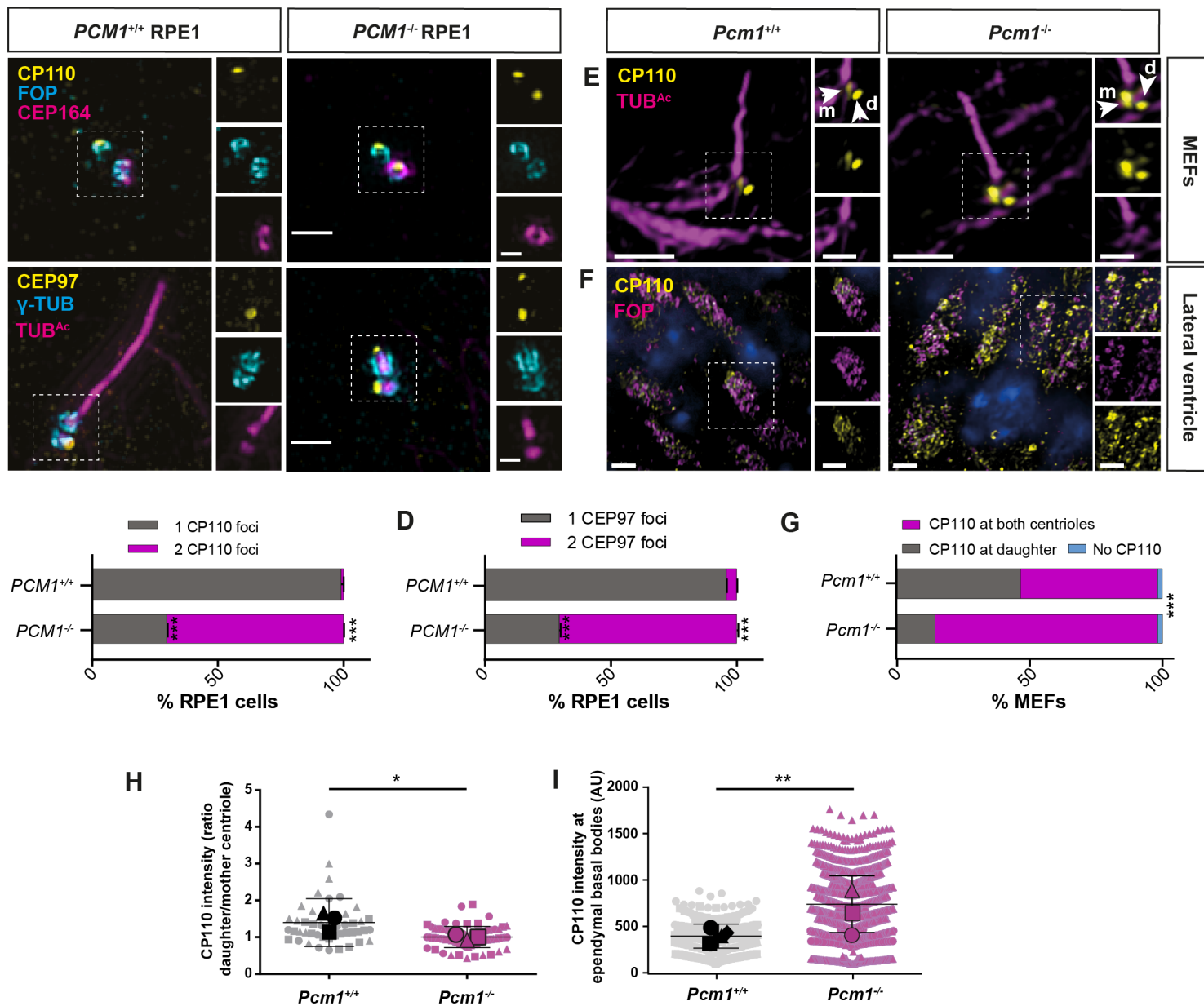


Figure 6

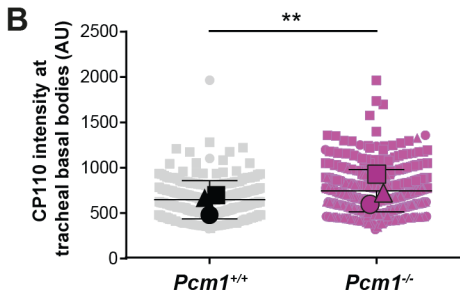
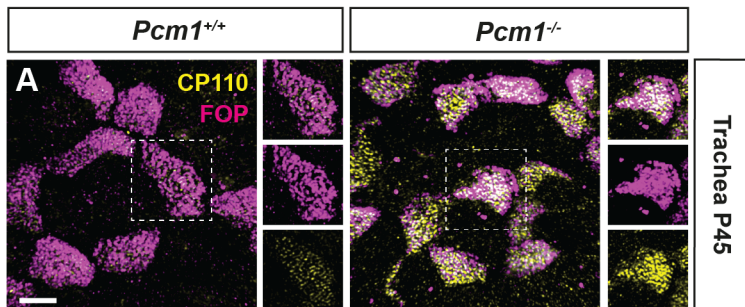


Figure 6 - figure supplement 1

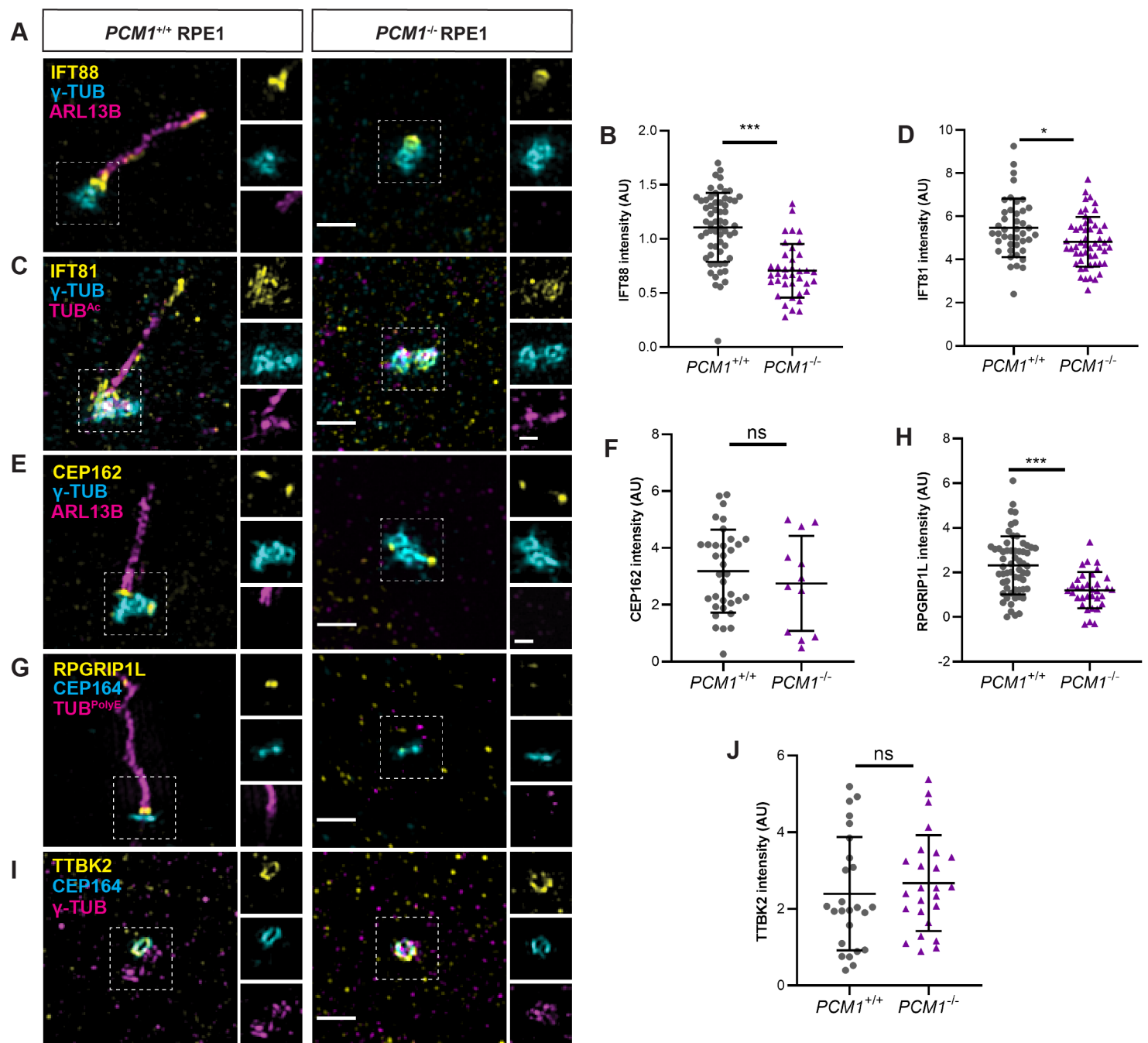


Figure 7

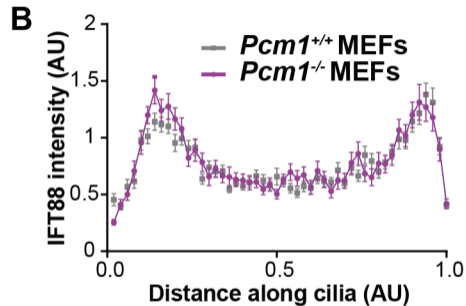
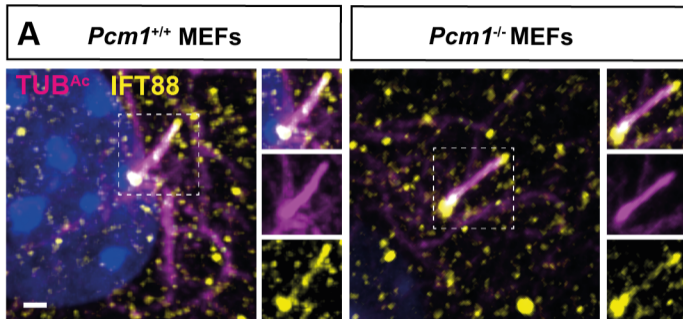


Figure 7 - figure supplement 1

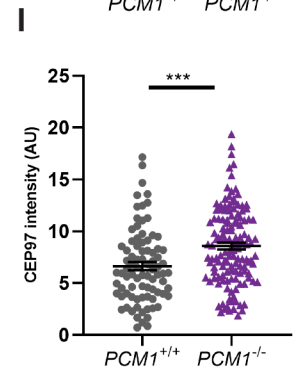
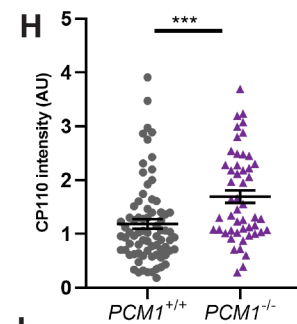
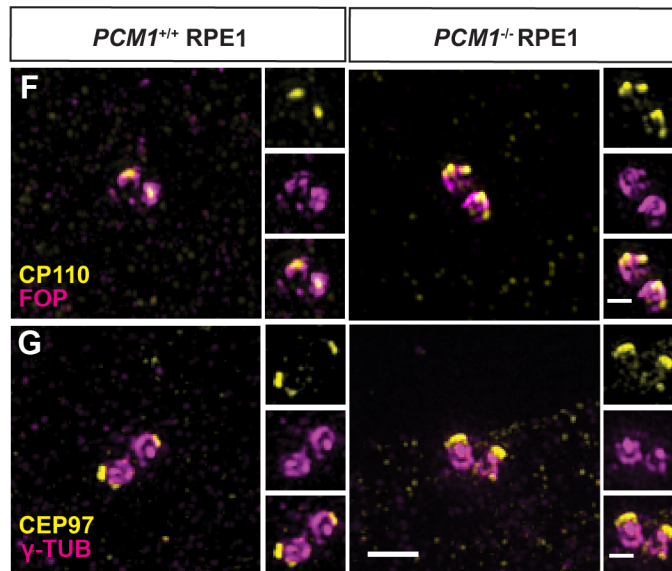
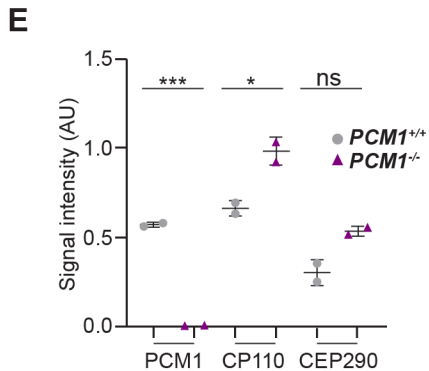
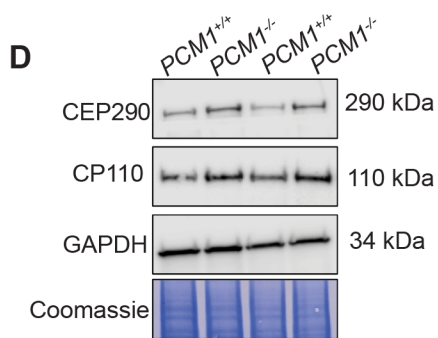
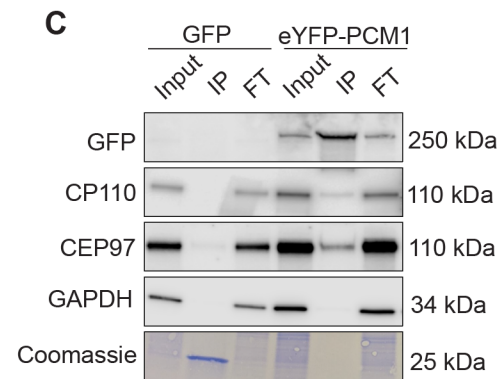
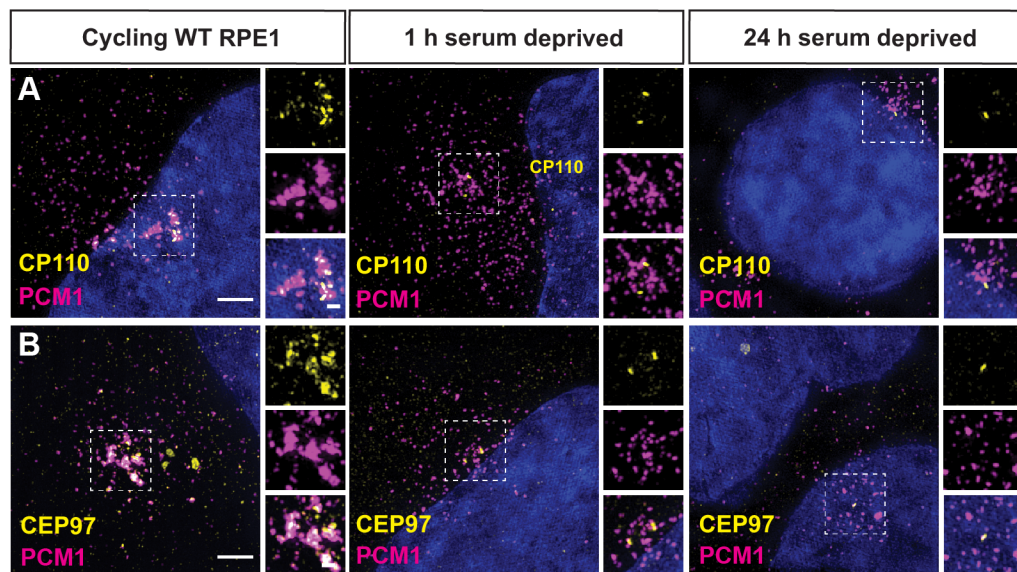


Figure 8

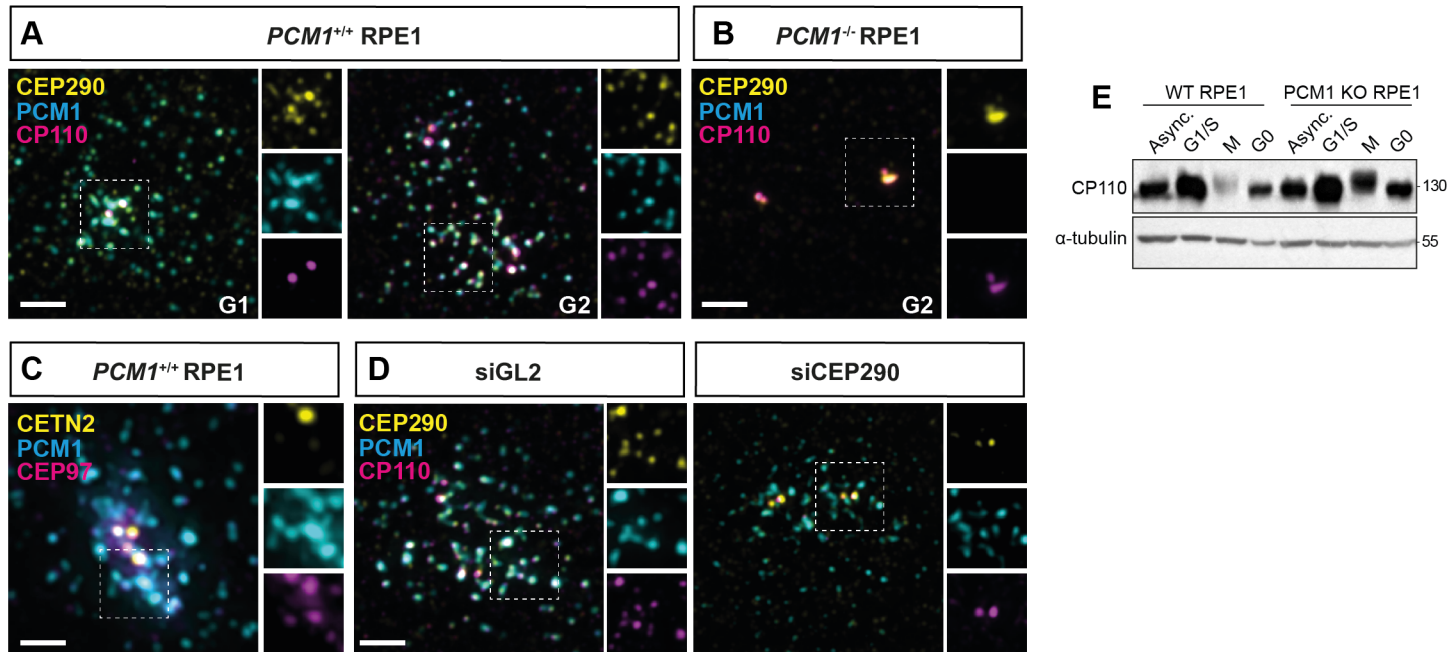


Figure 8 - figure supplement 1

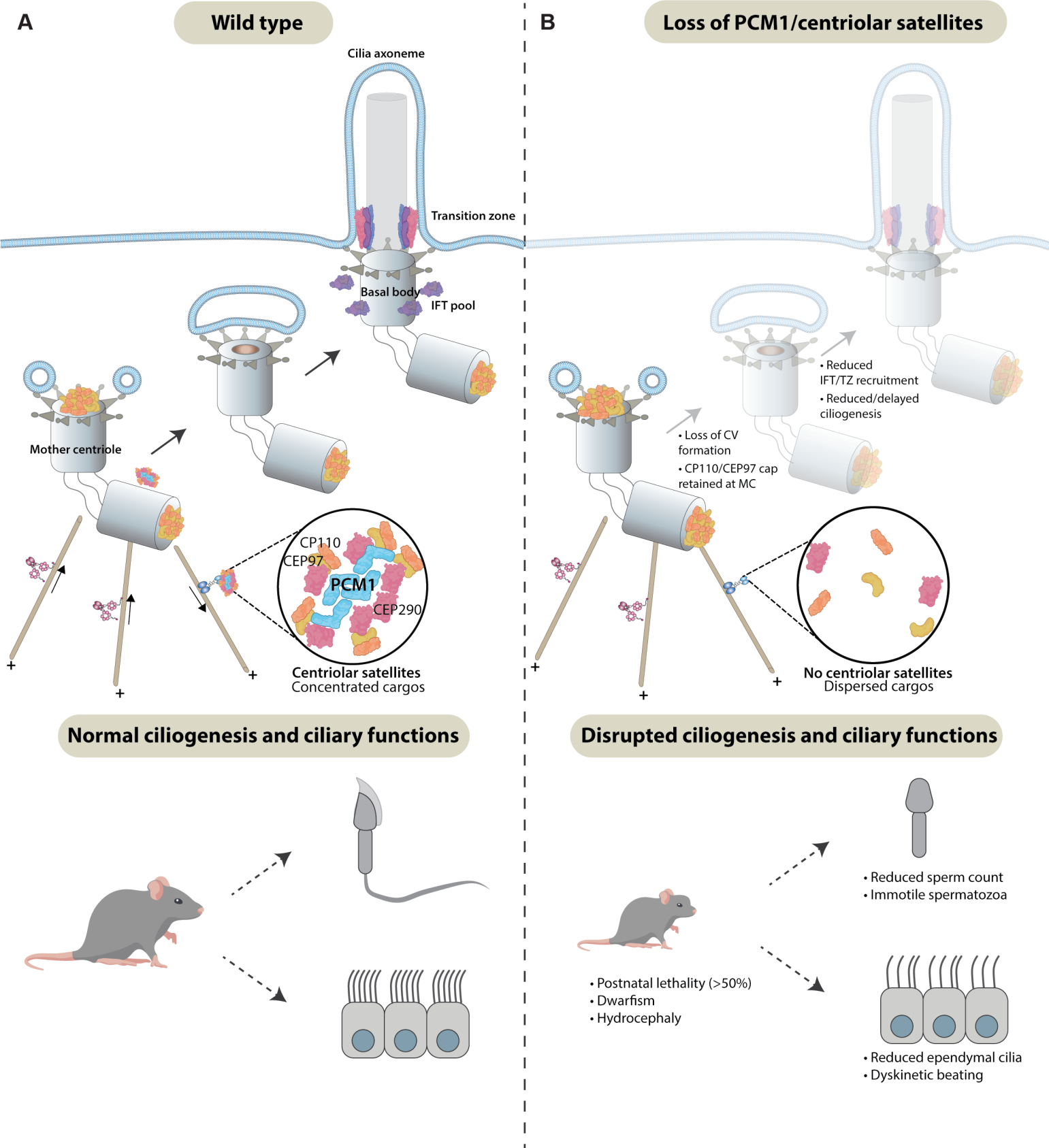


Figure 9